JGR Space Physics

RESEARCH ARTICLE

10.1029/2021JA030018

Key Points:

- We present an overview of 3 years of results from the search-coil magnetometer (SCM) on Parker Solar Probe
- The SCM reveals the magnetic signature of dust impacts and of slow extraordinary waves associated with type III radio bursts
- The SCM reveals in detail oblique whistlers and the radial evolution of turbulence at kinetic scales

Correspondence to:

T. Dudok de Wit,
ddwit@cnrs-orleans.fr

Citation:

Dudok de Wit, T., Krasnoselskikh, V. V., Agapitov, O., Froment, C., Larosa, A., Bale, S. D., et al. (2022). First results from the SCM search-coil magnetometer on Parker Solar Probe. *Journal of Geophysical Research: Space Physics*, *127*, e2021JA030018. https://doi.org/10.1029/2021JA030018

Received 7 OCT 2021
Accepted 21 MAR 2022

Author Contributions:

Conceptualization: G. Jannet
Data curation: C. Revillet
Formal analysis: T. Dudok de Wit, V. V. Krasnoselskikh, O. Agapitov, A. Larosa
Funding acquisition: P. Martin
Investigation: T. Dudok de Wit, V. V. Krasnoselskikh, S. D. Bale, T. Bowen, K. Goetz, G. Jannet, M. Kretzschmar, R. J. MacDowall, D. Malaspina, M. Pulupa
Methodology: T. Dudok de Wit, T. Bowen, B. Page
Project Administration: S. D. Bale, P. Harvey, P. Martin
Software: T. Dudok de Wit, T. Bowen
Supervision: T. Dudok de Wit
Validation: T. Dudok de Wit, C. Froment
Writing – original draft: T. Dudok de Wit, V. V. Krasnoselskikh, O. Agapitov, C. Froment, A. Larosa

First Results From the SCM Search-Coil Magnetometer on Parker Solar Probe

T. Dudok de Wit[1], V. V. Krasnoselskikh[1,2], O. Agapitov[2], C. Froment[1], A. Larosa[1], S. D. Bale[2], T. Bowen[2], K. Goetz[3], P. Harvey[2], G. Jannet[1], M. Kretzschmar[1], R. J. MacDowall[4], D. Malaspina[5,6], P. Martin[1], B. Page[2], M. Pulupa[2], and C. Revillet[1]

[1]LPC2E, CNRS, CNES, University of Orléans, Orléans, France, [2]Space Sciences Laboratory, University of California, Berkeley, Berkeley, CA, USA, [3]School of Physics and Astronomy, University of Minnesota, Minneapolis, MN, USA, [4]Solar System Exploration Division, NASA/Goddard Space Flight Center, Greenbelt, MD, USA, [5]Astrophysical and Planetary Sciences Department, University of Colorado, Colorado, Boulder, CO, USA, [6]Laboratory for Atmospheric and Space Physics, University of Colorado, Colorado, Boulder, CO, USA

Abstract Parker Solar Probe is the first mission to probe in situ the innermost heliosphere, revealing an exceptionally dynamic and structured outer solar corona. Its payload includes a search-coil magnetometer (SCM) that measures up to three components of the fluctuating magnetic field between 3 Hz and 1 MHz. After more than 3 years of operation, the SCM has revealed a multitude of different wave phenomena in the solar wind. Here we present an overview of some of the discoveries made so far. These include oblique and sunward propagating whistler waves that are important for their interaction with energetic electrons, the first observation of the magnetic signature associated with escaping electrons during dust impacts, the first observation of the magnetic field component for slow extraordinary wave modes during type III radio burst events, and more. This study focuses on the major observations to date, including a description of the instrument and lessons learned.

Plain Language Summary The search-coil magnetometer (SCM) search-coil magnetometer on Parker Solar Probe is an instrument that measures fluctuations of the magnetic field in the solar wind. The instrument covers frequencies ranging from 3 Hz to 1 MHz. After 3 years of operation the SCM has revealed a wealth of different wave phenomena. Here, we describe some of the highlights. These include whistler waves that propagate oblique to the magnetic field, the first observation of the magnetic signature associated with the impact of dust particles, and the first observation of the magnetic signature of high-frequency coherent waves that are associated with solar radio bursts.

1. Introduction

In November 2018 Parker Solar Probe (PSP) became the first satellite mission to penetrate deep into the inner heliosphere, below 0.29 AU, thereby opening new opportunities for studying in situ the young solar wind (Bale et al., 2019; Howard et al., 2019; Kasper et al., 2019; McComas et al., 2019). For its first solar encounter the perihelion was at 35.7 solar radii (0.17 AU) from the center of the Sun. From 2024 onwards, PSP will come as close as 9.85 solar radii (0.046 AU) from the Sun.

PSP addresses two fundamental problems in contemporary physics: coronal plasma heating and the acceleration of solar wind plasmas (Fox et al., 2015). To do so, the mission puts a strong emphasis on in situ observations of the upper solar corona. One of its four instrumental suites, called FIELDS, carries a series of instruments that can measure the electric and magnetic fields from DC to more than 1 MHz (Bale et al., 2016). FIELDS includes a Search-Coil Magnetometer (SCM) that measures magnetic field fluctuations between 3 Hz and 1 MHz (Jannet et al., 2021). Search-coils have a long heritage from missions in the solar wind, such as Helios (Neubauer et al., 1977), Cluster (Cornilleau-Wehrlin et al., 2003), Cassini (Gurnett et al., 2004), and Solar Orbiter (Maksimovic et al., 2020). The solar wind that is probed by PSP, however, is much less evolved as compared to what is usually observed near 1 AU. At the time of writing the final version of this manuscript, PSP has already performed 10 orbits around the Sun and the latest perihelion pass occurred on 21 November 2021 at a distance of 13.28 solar radii (0.062 AU).

After more than 3 years of operation, the SCM has observed a wealth of waves and transients. Some of them are new discoveries, such as the magnetic signature of dust impacts and a magnetic component for slow extraordinary waves associated with type III radio bursts. We felt that the time had come to provide an overview of some of these advances from an SCM instrument perspective and to mention some of the lessons learned.

This paper is organized as follows: after a presentation of the science case in Section 2, we present the instrument and its data products in Section 3. In the next sections, we focus on five examples. These are the observation of whistler waves (Section 4) and their spectral properties (Section 5), turbulence at kinetic scales (Section 6), the observation of the magnetic field component for slow extraordinary waves associated with type III radio bursts (Section 7) and the signature of dust impacts (Section 8). We conclude in Section 9 with some lessons learned.

2. Physical Background

One of the primary motivations for making AC magnetic field measurements in the solar wind is the characterization of magnetic fields fluctuations that can be either incoherent (e.g., Alfvén turbulence and signatures of reconnection events) or coherent (e.g., ion-cyclotron waves). Most of these fluctuations are driven by processes playing a major role in the heating and acceleration of a solar wind that has been found to be much more structured when approaching the Sun (Bale et al., 2019; Kasper et al., 2019).

Most of these processes are intimately related to the electron population, which is known to carry a major part of the heat flux in the solar wind. In particular, electrons play an important role in the energy balance during the expansion of the solar wind. Electron velocity distribution functions (VDFs) are highly non-thermal and typically have four components: (a) the core, which is a thermal and dense population that is, well represented by a bi-Maxwellian distribution, (b) a halo with a higher temperature and exhibiting strong high-energy tails, (c) an even hotter super-halo spanning up to a few hundred keV, and (d) a strongly anisotropic component, called strahl, which is aligned with the magnetic field (Pilipp et al., 1987; Rosenbauer et al., 1977). Suprathermal (i.e., halo, strahl, and super-halo) electrons are generally thought to originate in the solar corona (Pierrard & Voitenko, 2010; Štverák et al., 2009) and to propagate away from the Sun along interplanetary magnetic field lines. Collisions are known to keep the dense core population isotropic. This core cannot regulate the more tenuous higher energy electron populations such as the halo and strahl (Ogilvie & Scudder, 1978; Pilipp et al., 1987).

In this context, wave-particle interactions involving Magnetohydrodynamic (MHD) and kinetic scale waves (including whistlers) play an important role in dissipating energy. In the following we shall give particular attention to whistler waves, which play a key role in making the energetic part of the VDF evolve as the solar wind moves away from the Sun. Observations of the radial evolution of the electron VDF between 0.3 and 4 AU show that the number density of Strahl electrons (relative to the total number density) decreases away from the Sun while the relative number density of halo electrons increases and the core remains unchanged (Halekas et al., 2020; Maksimovic et al., 2005; Tao et al., 2016; Štverák et al., 2009). The opposite variations of the halo and the Strahl, and the fact that both cover the same energy range (100–1,000 eV) suggests that Strahl electrons may be pitch-angle scattered into the halo by a mechanism such as Coulomb collisions or by pitch-angle scattering by plasma waves propagating away from the corona (Horaites et al., 2015).

Another important problem in which wave-particle interactions play an important role is electron heat flux inhibition. The electron heat flux in collisionless or weakly collisional plasmas can be suppressed below the collisional Spitzer-Härm level (Spitzer & Härm, 1953). Heat flux inhibition mechanisms have fundamental applications in solar wind physics (Marsch, 2006). Spacecraft observations indicate that wave-particle interactions may inhibit the heat flux in the solar wind (Gary & Li, 2000; Scime et al., 1994). At sufficiently low Knudsen numbers the heat flux may be controlled by collisional processes only (Landi et al., 2014).

In the slow solar wind with velocities below 400 km/s, the heat flux is thought to be predominantly carried by halo electrons that are counter-streaming in the plasma reference frame. At sufficiently high values of the heat flux the so-called ”heat flux instability” is capable of generating whistler waves that propagate quasi-parallel to the heat flux (Gary et al., 1994). The unstable whistler waves may potentially suppress the heat flux scattering resonant electrons (Gary & Feldman, 1977). Observations of the saturation of the heat flux at a given β_e were interpreted in terms of a heat flux inhibition by whistler waves (Gary et al., 1994; Gary & Li, 2000). Simultaneous wave and particle measurements have recently confirmed that the heat flux instability indeed generates quasi-parallel whistler waves in the solar wind (Lacombe et al., 2014; Stansby et al., 2016; Tong, Vasko, Pulupa, et al., 2019). However, their role in suppressing the heat flux is still under active investigation.

Another source of instability, in addition to the heat flux, is the anisotropy of the core or halo distribution (Gary et al., 1994; Vasko et al., 2019). The role of this instability has been evidenced in the outer radiation belts of the Earth's magnetosphere. Its presence in the solar wind it is still under investigation (Jagarlamudi et al., 2020).

The situation is different in the fast solar wind in which a major part of the heat flux is carried by strahl electrons. The heat flux instability driven by counter-streaming core and halo populations (Gary et al., 1994) can still be excited in the fast wind. However, this instability is ineffective in suppressing the heat flux of strahl electrons because the associated quasi-parallel whistler waves interact efficiently only with electrons that propagate sunward. The mechanism of heat flux suppression in the fast solar wind must be associated with an instability that is driven by strahl electrons and produces waves that may scatter strahl electrons. The increase of the angular width of the strahl in velocity space with increasing radial distance from the Sun provides evidence for such a scattering process (Graham et al., 2017; Hammond et al., 1996). Statistical studies of the radial evolution of the electron VDF between 0.3 and 4 AU support this point of view, see for example, Graham et al. (2017); Štverák et al. (2009).

Wave-particle interactions have a crucial role in explaining the evolution of the VDF of the high energy electrons during the process of the formation of the both fast and slow solar wind. The major contributor in the regulation of the above described fundamental processes in the solar wind are whistler waves (Kajdič et al., 2016; Vocks & Mann, 2003). Whistler waves are right-handed polarized electromagnetic modes observed between the lower hybrid frequency f_{LH} and electron cyclotron frequency f_{ce} in the plasma frame. The range between these frequencies is often referred to as the whistler range since these waves are the dominant electromagnetic wave mode observed in this range. In the solar wind, whistlers are known to occur predominantly between f_{LH} and 0.5 f_{ce} (Lacombe et al., 2014). These waves have been studied onboard multiple spacecraft, such as Helios (Jagarlamudi et al., 2020), Cluster (Lacombe et al., 2014), Artemis (Stansby et al., 2016; Tong, Vasko, Artemyev, et al., 2019), and PSP (Agapitov et al., 2020; Cattell, Short, et al., 2021; Jagarlamudi et al., 2021).

The efficiency of whistler waves in diffusing energetic electrons strongly depends upon their amplitude, angle of propagation, *k*-vector, time duration, occurrence rate and frequency. These parameters determine which electron cyclotron resonances may be involved in wave-particle interactions in the inhomogeneous solar wind. These questions are further discussed in the context of the outer radiation belts of the Earth's magnetosphere by Artemyev et al. (2016). Here we shall address them using PSP observations.

PSP frequently observes enhanced wave activity in the vicinity of boundaries of switchbacks. The latter are sudden deflections of the magnetic field that are omnipresent at most perihelia (Bale et al., 2019; Dudok de Wit et al., 2020; Horbury et al., 2020; Kasper et al., 2019); they carry at their surface currents but also waves whose frequency is of the order of a few Hz (Krasnoselskikh et al., 2020; Larosa et al., 2020). The spatial location of these waves suggest that they may be located inside MHD discontinuities, as suggested earlier by Hollweg (1982). According to the latter author, the wavenumber vector of such waves should make an important angle with respect to the normal vector of the surface. Magnetic field measurements by the SCM provide a means for testing that hypothesis. As of today, however, the generation mechanism of these waves remains unclear.

At much higher frequencies, electromagnetic waves observed during type III radio bursts are of particular interest. The generation of such waves has been investigated for decades (Ginzburg & Zhelezniakov, 1958) and is now widely accepted to occur in two steps. First, energetic electrons that are accelerated in the lower solar atmosphere generate Langmuir waves; these waves are then scattered by ion density fluctuations and transformed into electromagnetic waves whose fundamental frequency is close to the plasma frequency (Voshchepynets et al., 2015). Harmonic couplings lead to harmonic emission (Freund & Papadopoulos, 1980; Krasnoselskikh et al., 2019; Papadopoulos & Freund, 1978, 1979; Tkachenko et al., 2021).

Most studies of these generation processes have been carried out by considering the primary waves that are generated by the electron beams as being electrostatic. However, in situ measurements of the electric field of these waves by WIND and STEREO spacecraft have revealed that the primary waves are actually electromagnetic (Bale et al., 1998; Kellogg et al., 1999). The evidence for this comes from the presence of a rotational component of the electric field of the wave. This result is not so surprising since theoretical studies have predicted that electrostatic Langmuir waves become slightly electromagnetic in the presence of a background magnetic field (Kim et al., 2013; Krauss-Varban, 1989). That is, they become electromagnetic with a large refractive index. As a consequence, the associated magnetic component should be small, though significant. This component has not been measured before in space plasmas because magnetic sensors rarely cover this frequency range. When they do, their sensitivity or their signal-to-noise ratio has been insufficient so far. One of the objectives of the SCM instrument is to carry out a systematic study of these waves, which have recently been observed for the first time (Larosa et al., 2022).

3. The SCM Instrument

3.1. Instrument Description

PSP has two different magnetic sensors: the Fluxgate Magnetometer (MAG) is a triaxial fluxgate magnetometer that covers the frequency range from DC to approximately 60 Hz (Bale et al., 2016) whereas the SCM is a triaxial search-coil magnetometer that measures magnetic field fluctuations between 3 Hz and 1 MHz. The analog signals of the SCM are amplified by a preamplifier that is located inside its foot, before being digitized and further processed by other instruments of the FIELDS suite (Bale et al., 2016). The heritage of this compact instrument is in the Demeter mission (Parrot et al., 2006); a similar search-coil is presently operating on Solar Orbiter (Maksimovic et al., 2020).

Each of the three antennas consists of a magnetic core with a winding whose voltage is proportional to the time-derivative of the magnetic field (Séran & Fergeau, 2005). Two antennas cover the 3 Hz–50 kHz frequency range (hereafter called LF, for low frequency). The third one is a dual-band antenna that covers both the LF and the 1 kHz–1 MHz) range (MF, for medium frequency). The antennas are 10.4 cm long and are mounted orthogonally on non-magnetic support. Jannet et al. (2021) provide a more thorough description of the instrument. In the following, (B_u, B_v, B_w) refers to the three components of the magnetic field in the instrument reference frame, and (B_x, B_y, B_z) in the frame of MAG. The double-band antenna measures B_u, which is approximately antiparallel to the ram direction of the solar wind.

To reduce the interference from stray electric fields, all sensitive parts of the SCM are wrapped in conductive layers: a 1 mm thick copper tube for the preamplifier and a flexible printed circuit for the antennas.

The SCM is located at the end of a 3.50 m boom, at the rear of the spacecraft. The instrument is never exposed to sunlight, except during short periods of off-pointing, when PSP is beyond the orbit of Venus. Because the search coil in the shade, needs to be heated to prevent its temperature from dropping below −50°C. When exposed to sunlight, its temperature typically reaches 10°C–50°C depending on the spacecraft's tilt angle.

3.2. Data Products

The analog outputs of the SCM are digitized and processed by three instruments: the Digital Fields Board (DFB; Malaspina et al. [2016]) can process all the LF and MF outputs whereas the Time Domain Sampler (TDS; Bale et al. [2016]) processes the MF output only. The latter can also feed into the Radio Frequency Spectrometer (RFS; Pulupa et al. [2017]) but this option has not yet been used.

The main data products are so-called survey mode waveforms of all three LF signals. Multiple sampling rates are possible, defined as 150 kHz/2^n where n is an integer. For most solar encounters the sampling rate is 292.97 Hz although some days have been sampled at 2,344 Hz after encounter 7. In burst mode, the sampling rate of DFB can reach up to 150 kHz. The registration of the waveforms of the LF B_u antenna has been discontinued after the occurrence of the anomaly (see Section 3.5) except when the sampling rate was high enough to capture a physical signal.

DFB also routinely produces auto-spectra and bandpass filtered amplitudes using the LF sensors. These data products also come with a large variety of operation modes. During the first encounter, when the LF B_u antenna was still working properly, DFB also collected 3 × 3 cross-spectral matrices, allowing the polarization properties to be investigated, see Section 5.

Spectral products are available in two frequency ranges: AC spectra cover the range from 366.2 Hz to 72.66 kHz and DC spectra range from 22.88 to 4,541 Hz. The number of frequency bins can be either 56 or 96. The bandpass filtered data also have two frequency ranges: the AC range goes from 878.9 Hz to 56,250 Hz and the DC range from 1.717 to 7,031 Hz, with respectively 7 and 15 frequency bins. Bandpass filtered data come in two versions: one with time-averaged values and one with peak values. Compared to spectra, they are available for one component only, and offer lower spectral resolution (and no cross-spectral products) but a higher cadence of 1.14 Hz throughout the whole encounter period.

A large fraction of the collected data so far consists of burst waveforms from the MF antenna, recorded by the TDS. These bursts typically have 32,768 samples and are sampled at 1.92 MHz; their trigger has been configured to detect dust impacts and intermittent waves such as Langmuir waves in the electric field. Examples of such waveforms will be given in Sections 7 and 8.

Finally, there is a merged magnetic field data product that combines the SCM and MAG waveforms (Bowen et al., 2020). The merging method is similar to the one used for the fluxgate and search-coil of the Magnetospheric Multiscale Mission (Fischer et al., 2016). The full data product is available for the first solar encounter only. For subsequent encounters, the merged magnetic field is available only for the B_v and B_w components.

Level 1 data products consist of uncalibrated data and are not publicly available. Level 2 data products are calibrated in physical units and become public after a few months. That is, data from orbit n become public when PSP is nearing the end of orbit $n + 1$. All level 2 and 3 data are publicly available, see the Data Availability Statement at the end of this article.

3.3. Instrument Sensitivity

One of the main challenges we faced during the design of the SCM was the large dynamic range that is required to accommodate both small-amplitude fluctuations of solar wind turbulence and large transients expected, for example, from shocks. Since the dynamic range of the instrument exceeds that of the instruments that process its analog output, the decision was taken to have a relatively low gain (compared to other missions in the solar wind) of $-50\,\mathrm{dBV/nT}$ in the Extremely Low Frequency and Very Low Frequency range. These points are detailed in Jannet et al. (2021).

A key characteristic of the instrument is the noise level or Noise Equivalent Magnetic Induction (NEMI), which is defined as the smallest amplitude an external magnetic induction with a frequency f should have in order to produce a detectable output signal that exceeds the instrumental noise level (Pfaff et al., 1998). The NEMI is usually represented in the spectral domain, see Figure 1. Its value is primarily constrained by the length of the antennas and the number of turns on each, both of which are dictated by the size and mass of the instrument (Jannet et al., 2021).

DFB has two gain modes that differ by a factor of 15. The high gain mode, which is the default one since launch, offers in the LF band a digital resolution that is equivalent to a 6 pT, with the largest possible amplitude of 185 nT. In low gain mode, the resolution is 15 times coarser and the largest amplitude is 2,990 nT. Digitization noise typically represents the equivalent of 1–2 bits. Note that because of the relatively low gain of the SCM the measurable levels are determined not only by the NEMI but also by the digital resolution of the DFB and the TDS, and by their digitization noise. That is, to determine the true noise level of the instrument, one should combine both the NEMI and the digitization noise. Unfortunately, the latter depends on the spectral properties of the signal and therefore cannot be represented by means of a simple curve in the frequency domain, as for the NEMI.

Figure 2 summarizes the main characteristics of the levels of magnetic field fluctuations that are observed by the LF B_v channel. The same conclusions hold for the LF B_w channel, whereas the LF B_u channel behaves differently, see Section 3.5. The radial scaling of the median and the 99th percentile of the fluctuation level both reveal the familiar R^{-2} scaling versus radial distance from the Sun. A key feature is the flattening of both curves beyond a given distance. The corresponding levels are well above the instrument sensitivity, and therefore cannot be attributed to the NEMI of the instrument or to the digital resolution; they are the signature of the omnipresent interference noise that comes from the spacecraft's reaction wheels. This interference noise is narrowband in frequency and therefore does not exclude the analysis of much weaker signals in the waveforms, as long as their

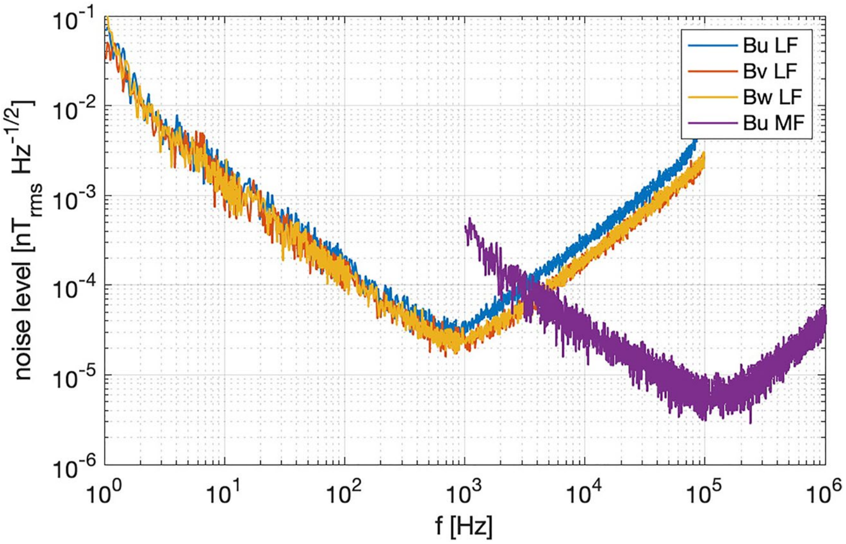

Figure 1. Noise level or Noise Equivalent Magnetic Induction (NEMI) of the search-coil magnetometer, measured before launch.

spectral bands do not overlap. This interference noise, however, cannot be properly eliminated from the spectral data products.

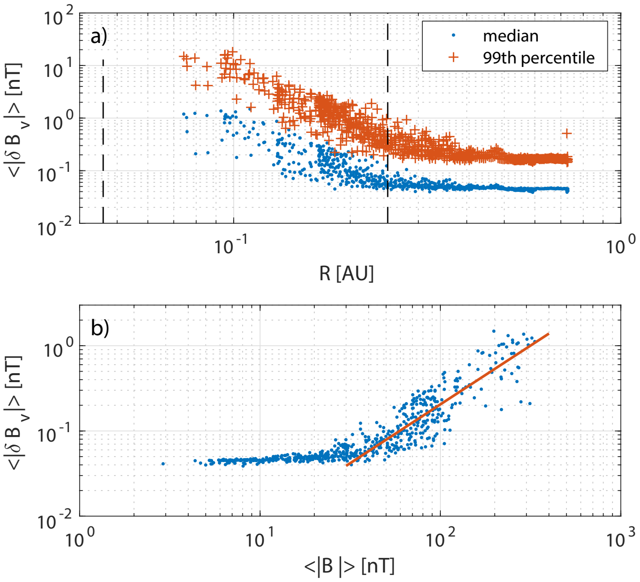

Figure 2. Main properties of the fluctuation level in the low frequency range with (a) the radial evolution of the fluctuation level $|\delta B_v|$ (using the median and the 99th percentile of that level) and (b) the relationship between the magnitude $|B|$ of the DC magnetic field and that of the fluctuation level $|\delta B_v|$. All quantities are estimated from 6-hr intervals, excluding those that have less than 10^6 samples or are corrupted by incorrect values. The vertical dashed lines in the plot (a) reveal the position of PSP's closest encounter with the Sun and the distance (0.25 AU) beyond which the SCM is not operating continuously. Most of the physically relevant observations occur between these two dashed lines. The oblique line in the plot (b) expresses a power law relationship (see text).

Figure 2a tells us that the routine analysis of fluctuations becomes more difficult beyond approximately 0.25 AU because interference noise is gradually overwhelming the plasma signal. The survey mode, however, is continuously turned on only within 0.25 AU only and during Venus encounters. A higher internal gain of the SCM could have improved the situation by reducing the effect of digitization but would not have solved the problem with interference noise.

Figure 2a also suggests that with a higher internal gain the SCM should still be able to capture the largest fluctuations that are expected during the closest solar encounters, with an occasional saturation. From the R^{-2} scaling, we expect levels (at the 99th quantile) of typically 100–500 nT whereas the instrument saturates at 185 nT in high gain mode. In hindsight, the internal gain of the SCM could have been an order of magnitude higher, allowing us to cover a wider amplitude range by switching between the two gain modes of the DFB.

Figure 2b compares the median fluctuation level to the magnitude of the DC magnetic field. This figure reveals two regimes: far away from the Sun, when the DC magnetic field is weak (typically below 30 nT), and the signal from the SCM is dominated by interference noise. Closer to the Sun, the fluctuation level increases proportionally to the DC magnetic field. The oblique line represents the best power law fit (in a least-squares sense, excluding values that are below the noise level) between the two, namely $\langle|\delta B_v|\rangle \propto \langle|\mathbf{B}|\rangle^p$. The value of the exponent, $p = 1.35 \pm 0.08$, suggests that the relative fluctuation level gradually increases when approaching the Sun. In contrast, this relative level is known to be approximately constant ($p = 1$) at larger distances, typically beyond 0.7 AU (Khabarova & Obridko, 2012). We interpret this difference as a signature of the un-evolved solar wind in the innermost heliosphere.

3.4. Instrument Calibration

An on-board calibration mode has been implemented in FIELDS, similar to that used on other missions such as the Magnetosphere Multiscale Mission (Le Contel et al., 2014). Just before and after each perihelion pass, the DFB generates a signal that is sent to the SCM counter-feedback winding through the preamplifier. This signal consists of 2 sine waves: one with a fixed frequency of 9.96 kHz and eight whose frequency is 9.96 kHz/2^n, where $n = \{1, 2, \ldots, 8\}$ (Malaspina et al., 2016).

The presence of this onboard calibration is motivated by the impact on the instrument of temperature variations occurring during the orbit. As of today, the observed variations in the gain and the phase of the instrument are within the confidence intervals of the observed response, which means that the characteristics of the instrument have not drifted since the launch in 2018 (apart from an anomaly in the LF B_u channel, see Section 3.5).

This lack of drift is not so surprising since the temperature of the antennas and of the preamplifier always stays near −50°C when the spacecraft is inside 0.25 AU. The sensor is then located in the shade of the spacecraft is, therefore, permanently heated, and has a constant temperature.

While the gains are absolutely calibrated, for the phases we only know the difference between the channels and not the absolute phase. Unfortunately, no complete end-to-end calibration of the system was carried out during integrations. While each subsystem was carefully calibrated, time was too scarce to properly check the full instrument chain.

The lack of system-level calibrations can be partly compensated by on-orbit observations. For example, the low-frequency part of SCM waveforms (frequencies below 100 Hz), as recorded by the DFB, is in very good agreement with the waveforms from the MAG fluxgate magnetometer, see (Bowen et al., 2020) and Section 3.6. For DFB burst waveforms whose frequencies can go up to 150 kHz, no such comparison is possible and other strategies are required. One of them consists in comparing the phase of whistler waves with waveforms of the electric field. This work is ongoing as small but significant phase anomalies persist at higher frequencies.

3.5. Anomaly of the LF B_u channel

The response of the LF B_u sensor suddenly changed between 3 and 4 March 2019. This anomaly happened shortly before PSP's second solar encounter when a rotation of the spacecraft was causing the SCM to move into shade after a period of direct exposure to the Sun. This anomaly has since arisen whenever the temperature inside of the instrument drops below 20°C. That is, whenever PSP is in a solar encounter phase.

The main manifestation of this anomaly is a sudden loss of sensitivity of the LF B_u sensor as if an additional first-order high-pass filter with a cutoff around 1 kHz had been added to the output of the preamplifier. This change also affects the phase. A second manifestation is an increase of more than two orders of magnitude of the level of interference noise that comes from the cycling of the current pulses that heat the SCM preamplifier. The cycling has a period of typically 500 s. Under normal conditions, the magnetic signature of these current pulses remains hidden in the plasma signal. Since there is a weak cross-talk between channels (of the order of −30 dB, depending on the channels), the signature of heater noise has moderately increased too in the B_v and B_w channels.

The most likely cause for this anomaly is thermal stress, leading to the rupture of a wire inside of the 3D preamplifier with the LF B_u antenna becoming capacitively coupled whenever the instrument turns cold. Fortunately, there has been no impact on the properties of the other channels, and the degraded response of the LF B_u channel has since remained stable.

The main consequence of this anomaly is the impossibility to retrieve the full 3D spectral matrix (except for encounter 1). Therefore, properties such as wave polarization and ellipticity can be determined for encounter 1 only.

3.6. Intercalibration With MAG

One of the mission objectives is to measure magnetic field fluctuations from DC up to 1 MHz. The lower part of this frequency range is covered by the MAG fluxgate magnetometer (Bale et al., 2016), which covers the range

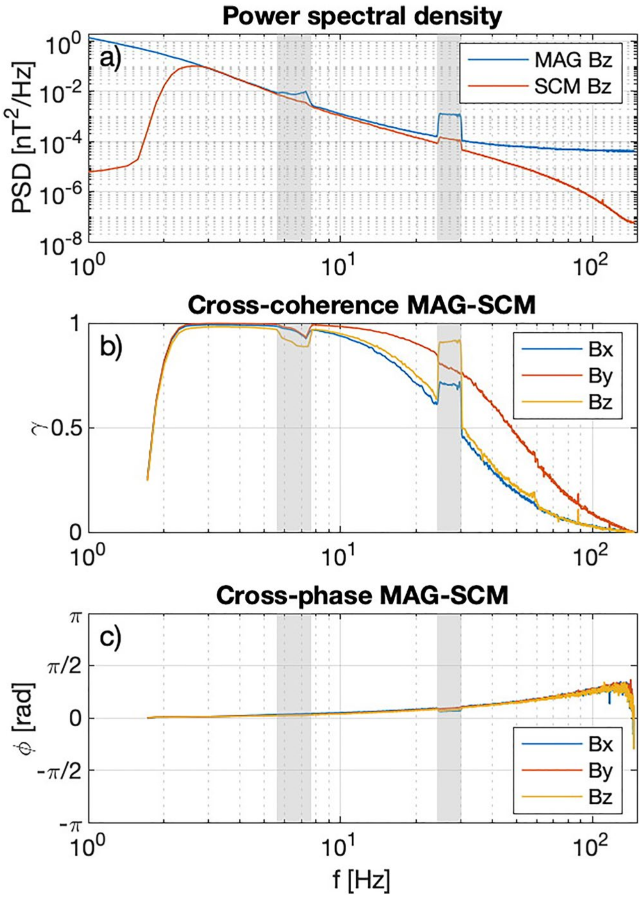

Figure 3. Comparison of the spectral properties of Fluxgate Magnetometer (MAG) and the search-coil magnetometer (SCM), with (a) the power spectral density of their B_z component, (b) the cross-coherence γ between all three pairs of components, and (c) the associated cross phase ϕ. These properties are estimated from waveforms that are captured on 5 November 2018, between 00:00 and 15:27 UT and sampled at 293 Hz. We use the rotation matrix of Equation 2 to express the waveforms from the SCM in the reference frame of MAG. Spectral bands with interference from the reaction wheels are shaded.

from DC to approximately 60 Hz. The SCM covers frequencies above 3 Hz. The waveforms from both instruments have been combined into one single waveform that is available as a level 3 data product (Bowen et al., 2020).

Figure 3 illustrates some of the aspects of the intercalibration by comparing the power spectral densities and cross-coherences between both instruments for observations made near the first perihelion pass when the signals had a favorable signal-to-noise ratio. The upper plot compares the power spectral densities of the calibrated waveforms from both instruments, showing the low frequency cutoff at 3 Hz for the SCM and the gradual appearance of incoherent noise in MAG data, with a noise floor above approximately 60 Hz. The two discontinuities in the shaded frequency intervals are signatures from two of the four reaction wheels; their frequency slowly drifts during the time interval, hence the step-like pattern. Each reaction wheel spins at a different frequency. MAG and the SCM detect their fundamental tone and their harmonics, which sometimes reach hundreds of Hz.

An important result in Figure 3a is the good match in spectral response between the two instruments, for the frequency range in which they overlap well, given that they have been calibrated independently. What the logarithmic scale does not immediately reveal is a systematic difference in the responses, with slightly weaker values for the SCM. This difference ranges from 0.5 dB (for the B_z component) to 8 dB (for the B_x component). As of today, we have no clear explanation for this difference.

Figure 3b compares the cross-coherence between both instruments for all three components. Ideally, the cross-coherence should be equal to 1 for the spectral contents to be identical (regardless of gain differences). From this, we conclude that the frequency range in which the two instruments agree best is between 3 Hz and approximately 10 Hz. Above that frequency, the presence of noise in MAG cannot be neglected anymore. Below 3 Hz the gain of the SCM is too low.

Figure 3b shows that at high frequency the cross-coherence is relatively larger for the B_y component: this is a consequence of the rotation matrix R that is needed to rotate the magnetic field from *uvw* coordinates (the SCM frame) to the *xyz* coordinates (the MAG frame). We have

$$\begin{pmatrix} B_x \\ B_y \\ B_z \end{pmatrix} = \mathsf{R} \begin{pmatrix} B_u \\ B_v \\ B_w \end{pmatrix} \tag{1}$$

with

$$\mathsf{R} = \begin{pmatrix} 0.8165 & -0.4083 & -0.4083 \\ 0 & -0.7071 & 0.7071 \\ -0.5773 & -0.5773 & -0.5773 \end{pmatrix} \tag{2}$$

These equations reveal that the B_y component is a linear combination of B_v and B_w whereas the other components require B_u, B_v, and B_w. For that reason, assuming that the noise is independent in each channel, the B_y component should have a noise variance that represents approximately 2/3 of that of the other components and therefore exhibit a higher cross-coherence with the B_y component from MAG.

Finally, we compare in Figure 3c the cross-phase between both instruments. The weak but significant linear increase with frequency suggests that there is a small residual delay between the SCM and MAG, which has not been accounted for. The delay represents a quarter only of a sampling period. The presence of this residual delay highlights again the importance of carrying out a system-level calibration before launch.

Note that the spectral signature of the interferences is quite different in both instruments (and also between the outboard and inboard MAGs) because they are located at different distances from the reaction wheels. This property can actually be used to help better remove the signature from reaction wheels, which pollutes the spectrograms. Although we have tested this, the feature has not been implemented in the data products.

4. Example: Whistler Waves, Waveform Observations

Let us now focus on a series of examples that highlight some of the observations that were made during the first 9 solar encounters. Some of these present original results while others are based on published results. We start with an example that has been discussed by Agapitov et al. (2020).

The frequency range in which MAG and SCM observations overlap exhibits different types of high-amplitude waves. Ion-cyclotron waves, which generally occur between 1 and 10 Hz have already been investigated in detail by several (Bowen et al., 2020; Chaston et al., 2020; Verniero et al., 2020). A different type of wave occurs above the local lower hybrid frequency f_{LH}, which was typically 20 Hz during the first perihelion. These waves are often observed inside dips of the magnetic field, which are associated with the boundaries of switchbacks (Agapitov et al., 2020; Drake et al., 2021; Farrell et al., 2020; Froment et al., 2021; Larosa et al., 2020; Mozer et al., 2020). The latter are sudden deflections of the magnetic field, which are omnipresent in the slow alfvénic solar wind and have received considerable attention.

Figure 4 presents a typical example of such a wave burst that occurs during a magnetic hole with a relative depletion of approximately 0.45 of the background field (Figure 4a). Here, the dip is located at the leading edge of a switchback, which occurs from 15:21-15:45 UT. The spatial scale of the magnetic depletion is typically 2,000 km (150 Larmor radii). The MAG and SCM waveform components are shown in Figure 4b. As already discussed in Section 3.6, the two instruments agree well in the frequency range in which they overlap; note that the SCM has a low frequency cutoff at 3 Hz. A polarization analysis reveals a right-handed circular polarization of the magnetic field and an elliptical polarization of the electric field with a $\pi/2$ phase shift. A comparison with the phase of the electric field waveforms from FIELDS shows that the oscillations of B_x and E_y are in-phase whereas B_y and E_x are out-of-phase. Further analysis indicates that the electromagnetic wave propagates along the background magnetic field and toward the Sun. The electromagnetic nature of the perturbation, its right-hand circular polarization, and the wave frequency range suggest that the observed perturbation is a whistler wave that is propagating toward the Sun both in the plasma frame and in the spacecraft frame. More details can be found in (Agapitov et al., 2020). Here, the wave propagates quasi-parallel to the background magnetic field. However, cases with oblique sunward propagation have also been reported (Agapitov et al., 2020).

The dynamic spectrum of Figure 4c shows a complex inner structure of the wave packet, which consists of a series of bursts. The stable wave phase relationship of the SCM magnetic field and the electric field waveforms allows the accurate processing of the radial component of the Poynting vector. The sign of the radial component of the Poynting vector changes from positive (sunward) at high frequencies to negative (anti-sunward) at lower frequencies, where MHD waves are observed. The wave frequency in the solar wind plasma frame, as reconstructed from the Doppler shift and the local parameters of plasma, is found to be in the range of 100–350 Hz, which corresponds to 0.2-0.5 of the local electron gyrofrequency f_{ce} (Figure 4d). Incidentally, the reconstructed wave frequency can be used to accurately calibrate the electric field measurements, and determine the effective length of the electric field antennas, which was found to be approximately 3.5–4.5 m in the 20–100 Hz frequency range (Agapitov et al., 2020; Mozer et al., 2020).

While each whistler wave packet has its own characteristics, the frequent occurrence of such waves during periods of the quiet solar wind, and in particular at the boundary of switchbacks, suggests that they are an important component of the solar wind. Interestingly, the population of such sunward propagating whistlers can interact efficiently with the energetic particles of the solar wind and affect the Strahl population, spreading their field-aligned pitch-angle distribution through pitch-angle scattering. For sunward propagating whistlers around 100–300 Hz,

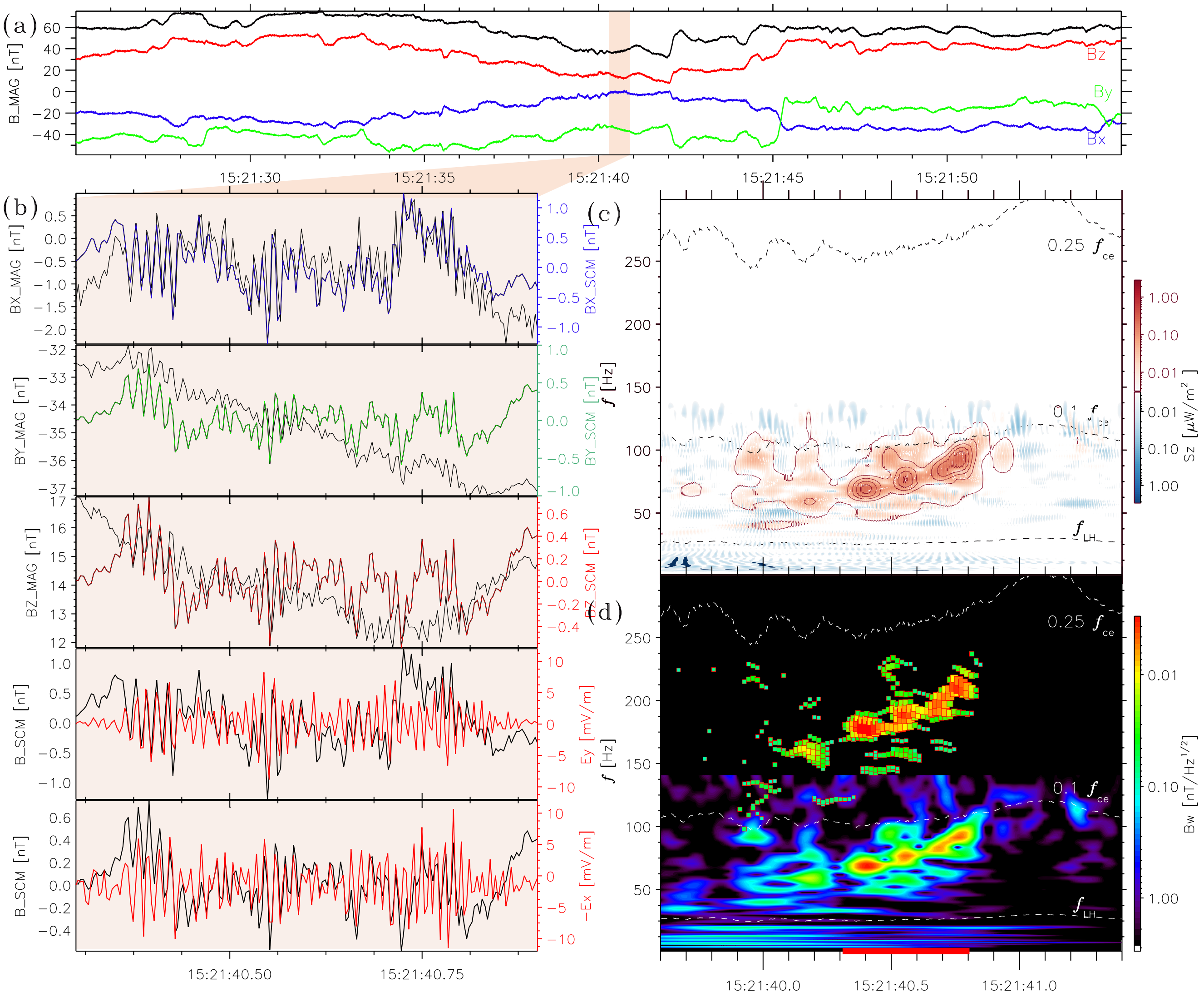

Figure 4. Whistler wave burst observed by Parker Solar Probe on 4 November 2018 during a dip of the magnetic field, with (a) components and magnitude (black curve) of the background magnetic field, as measured by Fluxgate Magnetometer (MAG) (b) Excerpt with waveforms of the magnetic field as observed by MAG and search-coil magnetometer during a 0.6 s interval; (c) Time-frequency representation of the radial component of the Poynting flux (sunward is in red, anti-sunward is in blue. This 1.8 s interval is longer than the one shown in (b), whose span is indicated at the bottom by a red bar; (d) Scalogram of the magnetic field in the satellite frame; the reconstructed power spectral density in the plasma frame is represented by colored squares. The lower hybrid frequency and fractions of the electron cyclotron frequency are indicated by dashed lines.

the resonance conditions occur for electrons with energies between approximately 50 eV and 1 keV. This energy range coincides with that of the observed Strahl (Halekas et al., 2020) and may potentially scatter Strahl electrons. Such an interaction can be even more effective if we take into account that some of the observed waves are oblique. For these waves, the effective scattering is strongly enhanced at higher-order resonances (Agapitov et al., 2014; Artemyev et al., 2016), which leads to a regulation of the heat flux (Roberg-Clark et al., 2018, 2019), and to an increase in the fraction of the halo distribution with the distance from the Sun (Halekas et al., 2020; Maksimovic et al., 2005; Štverák et al., 2009).

5. Example: Whistler Waves, Spectral Properties

Let us now focus on the spectral properties of whistler waves, using results that will be detailed in a forthcoming publication.

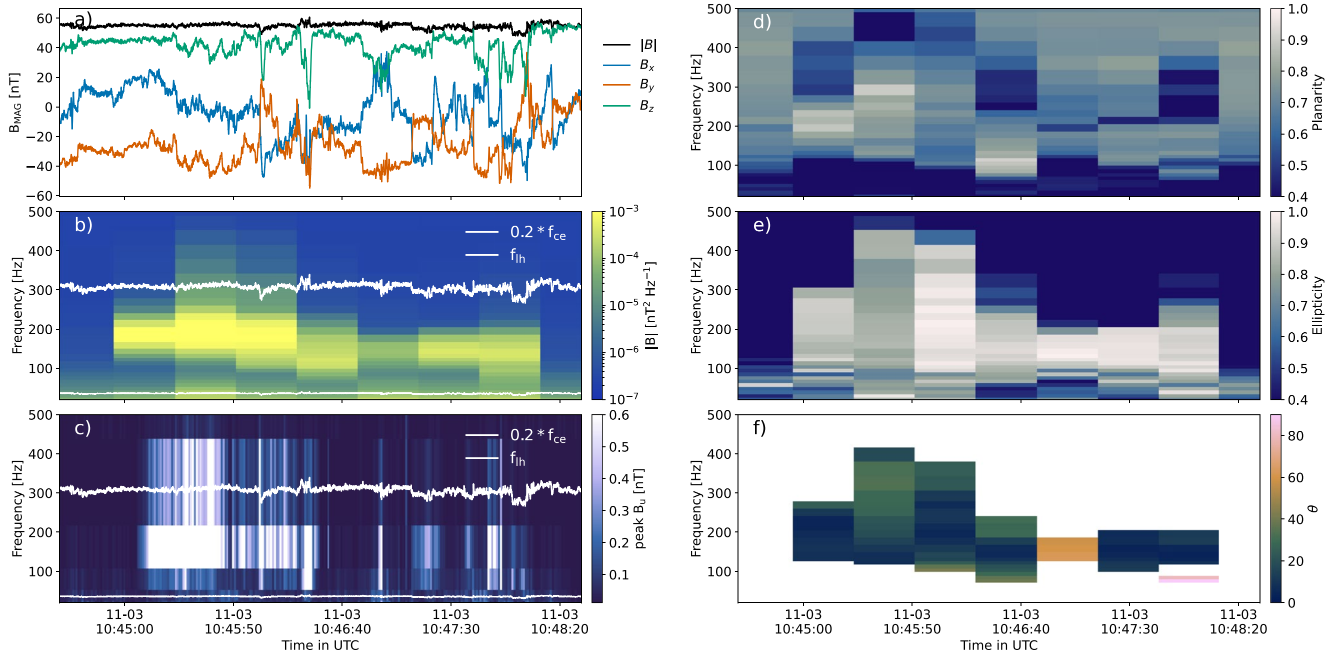

Figure 5. Whistler waves observed with spectral data on 3 November 2018. The panels on the left show, starting from the top: (a) the solar wind background magnetic field components (spacecraft frame) and magnitude from the Fluxgate Magnetometer instrument, (b) the trace of the cross-spectral matrix, (c) the peak value of the corresponding band-pass filtered measurements for the single component i.e., available for this data product. On both panels (b) and (c), the two white lines indicate 20% of the electron-cyclotron frequency f_{ce} and the lower-hybrid frequency f_{lh}, respectively. On the right, the panels show the polarization properties derived from the cross-spectra using the SVD technique: (d) planarity, (e) ellipticity, and (f) θ: the angle between k-vector and the solar wind background magnetic field. Only θ values for planarity and an ellipticity above 0.6, and significant spectral power above the ambient fluctuation level are displayed.

During PSP's first encounter with the Sun, that is, from 31 October 2018–12 November 2018, DFB continuously produced cross-spectra from SCM's three channels. These data include the real and imaginary parts of the six possible combinations of spectral cross products. This is a valuable dataset for studying the polarization properties of electromagnetic waves such as whistler waves, and for estimating how their properties evolve with different solar wind conditions and radial distances from the Sun.

Cross-spectra gives access to most of the range of whistler wave frequencies $f_{lh} < f < f_{ce}$, where f_{lh} is of the order of a few Hz to a few tens of Hz while f_{ce} can reach a few kHz for these solar wind conditions. DFB also recorded several tens of burst waveforms per day at 150 kHz; outside of these burst intervals, however, the sampling rate of the waveforms was at best 292.97 Hz. Farther away from perihelion, the sampling rate was even lower, which severely limited our ability to properly detect whistler waves. Under these conditions, cross-spectra are essential for doing polarization analysis.

Figure 5 presents an example of a whistler wave burst that was detected in cross-spectral measurements. As we will detail later, this example shows a variety of wave characteristics such as duration, wave normal angles, etc. The trace of the cross-spectral matrix shown in Figure 5b reveals significant spectral power, at least four times the ambient fluctuation level, for seven consecutive 28-s bins, that is, for 3.3 min in total. The median frequency of these wave packets is about 156 Hz, that is, 0.1 f_{ce}. We investigate the polarization properties of these fluctuations by means of the singular value decomposition (SVD) technique (Santolík et al., 2003) to confirm that these are coherent and plane waves. The high levels of near-circular polarization in Figure 5e together with the frequency range support the idea that these are whistler waves, and not turbulence.

The determination of the angle between the k-vector and the background magnetic field (which we call θ) is an important step in the study of whistler-electron interactions in the solar wind (see Section 2). However, cross-spectra are recorded at a relatively low cadence as compared to the characteristic timescale of the fluctuations in the DC magnetic field. As can be seen in Figure 5a, the background magnetic field can substantially evolve during one single 28-s bin. Sometimes, as shown in Section 4, whistler waves in the young solar wind coincide with magnetic dips or with the boundary of deflections called switchbacks. Using bandpass filtered measurements, Jagarlamudi et al. (2021) and Cattell et al. (2021) have further confirmed that these whistler waves are highly intermittent.

In summary, in order to obtain a correct estimate of θ, it is crucial to select, for each cross-spectral bin, the most representative value of the background magnetic field, taking into account the occurrence of whistlers in the bins. In practice, we have chosen to weigh the average background magnetic field by the power spectral density estimated from the peak value of the bandpass filtered measurements (see Section 3.2). The bandpass filtered measurements represent the amplitude of the wavefield (here the peak amplitude) in specific spectral bands, as can be seen in Figure 5c. The 0.8-s cadence of the bandpass filtered data allows us to confidently estimate the background magnetic field at the time of the whistler wave packets for which we see a signature in the (larger) cross-spectral bins. We tested this technique with examples for which waveforms were available, in order to validate the results. The same procedure has been used by Froment et al. (2021). Figures 5b and 5c show a variety of configurations that were encountered, with cross-spectral bins that correspond to a quasi-continuous signature in the bandpass filtered peak value and cross-spectral bins with very sporadic signatures in the bandpass filtered data.

The panels on the right of Figure 5 show the result of a polarization analysis, with a high planarity and ellipticity, and a diverse range of obliquity of the wave packets. Here, the angle θ has a 180° ambiguity that can be lifted by using electric field measurements in burst mode, when available. Most wave packets are quasi-parallel ($\theta < 45° \pm 180°$). Some wave packets are significantly oblique and show $\theta \sim 60° \pm 180°$ and $\theta \sim 90° \pm 180°$, that is, with angles that are close to the resonance cone. Similarly, most of the whistler wave packets that are detected in cross-spectral data during the first encounter are quasi-parallel. Only a few percent are oblique as it will be detailed in a forthcoming study.

Although the propagation direction of whistlers is expected to be approximately collinear with the background magnetic field, oblique whistlers have been observed in simulations (Vasko et al., 2019) and in observations (Agapitov et al., 2020; Cattell et al., 2020). The simulated wave packets were found to be predominately electrostatic whereas the observed oblique whistlers had relatively large amplitudes. The obliquity is of particular interest since several authors have reported for PSP a broadening of the Strahl concurrent with the presence of whistler waves (Cattell et al., 2021; Jagarlamudi et al., 2021). Although the exact origin of these wave-particle interactions is still uncertain, the interactions themselves are expected to play an important role in the regulation of electron heat flux.

Finally, in this example, the maximum relative peak amplitude $|\delta B_u|/B| = 0.04$ is an order of magnitude larger than what has been reported near 1 AU (Cattell et al., 2020; Tong, Vasko, Artemyev, et al., 2019), which is consistent with other studies of PSP observations (Agapitov et al., 2020; Cattell, Short, et al., 2021).

6. Example: Turbulence at Kinetic Scales

In the last decade, there has been considerable interest in the high-frequency end of solar wind turbulence, where the MHD approximation is no longer valid (Bruno & Carbone, 2013; Verscharen et al., 2021). Unlike the inertial range of turbulence, whose power spectral density is a power law with one single spectral index, the kinetic range of turbulence is characterized by multiple breaks in the power spectral density with different slopes in between. A key feature is the steepening of the spectral slope in sub-ion scales with a spectral index that is often found to be around −2.8. Of particular interest is the radial evolution of these properties as this should help identify what drives these spectral breaks and, more generally, how the energy dissipation occurs between ions and electrons.

Using search-coil data from PSP's first solar encounter, Bowen, Mallet, et al. (2020) have confirmed the steepening of the spectrum above ion-kinetic scales (above 1 Hz) with a significant dissipation of the turbulent energy flux in this range of scales. Huang et al. (2021) likewise have revealed the presence of different spectral breaks with spectral slopes that depend on the amplitude of the fluctuations. Measurements made during PSP's first two Venus gravity assists (in October 2018 and December 2019) confirm the presence of developed kinetic turbulence in the planets magnetosheath and the role played by ion-scale instabilities (Bowen et al., 2021). As for higher-or-

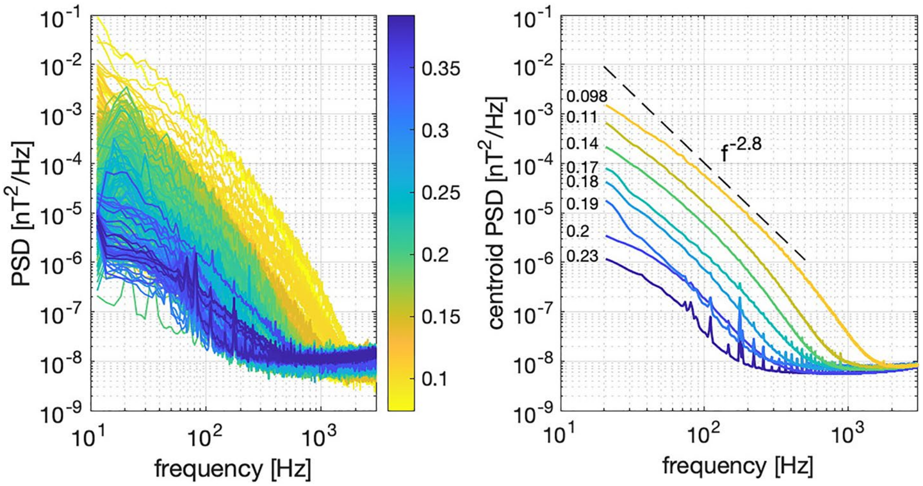

Figure 6. Power spectral density of the B_v component for solar encounters 1 to 8, excluding bursts with interference or with signatures of wave activity. The plot on the left shows all 2789 spectra, with a color coding that reflects the distance to the Sun in AU. The plot on the right shows 8 centroids obtained by k-means clustering, that is, Eight representative spectra. For each of them, the median distance to the Sun is indicated in AU. A power law with a spectral index of −2.8 is also shown to guide the eye (dashed line).

der statistical properties, they reveal the transition from multifractal scaling in the inertial range, to monofractal scaling in the sub-ion range, with the possible role of current sheets at sub-ion scales (Chhiber et al., 2021).

One of the key issues here is the identification of the dominant dissipation mechanisms, for which a radial scan of the properties of kinetic turbulence should help disentangle different physical drivers. The two main competing views involve either the presence of several spectral breaks with self-similar scaling in between (Sahraoui et al., 2009, 2013) or a universal scaling with an exponential cutoff (Alexandrova et al., 2009, 2012). The reanalysis of search-coil observations made by Helios between 0.3 AU and 0.9 AU shows evidence for a universal scaling law in which the electron gyro-radius scale sets the end of the turbulent cascade (Alexandrova et al., 2021). These data, however, offer poor frequency resolution and come with some technical issues.

One of the main challenges in the analysis of magnetic fluctuations in the kinetic range is the omnipresence of whistler wave instabilities which, coincidentally, happen to occur in the same frequency range. For observations made by PSP their doppler-shifted frequency typically ranges between 30 and 300 Hz. To exclude intervals that are polluted by whistler waves, we focus on waveforms and consider high cadence bursts recorded by the DFB Burst Memory (DBM). Each burst has three components of the magnetic field, typically with 507,905 samples that recorded at 150 kHz. For solar encounters 1 to 8 we collected 7440 valid burst events in high gain mode. Some events are also available in low gain mode but were discarded here because of their poorer signal-to-noise ratio. The results that are presented below are original.

Figure 6 illustrates a subset of 2789 events without significant levels of coherent wave activity (such as whistler waves), showing the power spectral density of the B_v component for solar encounters 1 to 8. Most of these events were recorded in slow alfvénic winds. Notice the characteristic gradual steepening the signal before it hits the noise floor near 1×10^{-8} nT^2/Hz. The corresponding range of cyclotron frequencies for the different solar encounters is 1–8 Hz for ions and 2–10 kHz for electrons.

To highlight the radial evolution of the shape of the power spectral density, instead of binning the spectra into different radial intervals we perform a k-means clustering, see the right plot of Figure 6. Averaging the binned spectra tends to smear out the variability in the spectral breaks, which we are precisely interested in. Clustering, on the contrary, extracts a set of representative spectra, called centroids. There is no well-defined optimum number of clusters here, so we select eight of them, to reveal a range of variability. Our conclusions remain unchanged if we use more clusters.

Figure 6 confirms the gradual steepening of the power spectral density, which had already been observed at 1 AU at lower frequencies (Kiyani et al., 2015), and deeper inside the heliosphere with Helios (Alexandrova et al., 2021), with limited frequency resolution. However, with PSP we find that this steepening does not show clear evidence for one single parametric shape. In particular, it does not reveal a double power law as in (Sahraoui et al., 2013), nor does it reveal a power law with an exponential cutoff as in (Alexandrova et al., 2021). These results suggest that the radial evolution of the turbulent cascade in the kinetic range is more complex than what is observed farther away from the Sun. They also suggest that the spectral index may not be the most pertinent parameter since what matters are physical properties such as the spectral energy transfer rate between scales and also the difference between the time taken for waves to propagate away from their source region and the nonlinear interaction time between waves.

7. Example: Magnetic Signature of Type III Radio Bursts

Quasi-monochromatic waves occurring near the plasma frequency have been routinely observed in the solar wind since the early observations by Scarf et al. (1971) and by Gurnett and Frank (1975). These waves are generally observed in the vicinity of bow shocks (Kellogg, 2003) or are associated with type II or type III radio bursts (Kellogg et al., 1999). A major step forward in their understanding was made when their association with energetic electrons was discovered (Lin et al., 1981). Today, it is widely accepted that these electromagnetic waves are generated through mode conversion of electrostatic Langmuir waves; the details, however, are not yet fully understood, see Section 2. Until recently, no direct evidence for the magnetic signature of these waves had been found, except for early observations by Scarf et al. (1970, 1971) with the OGO 5 spacecraft; unfortunately, their interpretation had remained ambiguous. In May 2020, however, PSP revealed the first magnetic signature of the Langmuir-slow extraordinary wave mode in high-frequency waveforms. Here, we illustrate this finding, which is further discussed in Larosa et al. (2022).

The instrument that is best suited for analyzing high-frequency waveforms near the plasma frequency is the Time Domain Sampler (TDS; Bale et al. [2016]), which captures waveforms in 5 channels with a cadence up to 1.92 MHz. In its usual operating mode, TDS captures tens up to hundreds of bursts per day, each of which has 32,768 samples and lasts for 17.1 ms. The triggering algorithm of these bursts has evolved during the mission, being more sensitive to dust impacts during the first encounter, and after that tuned to detect more Langmuir waves. One of the channels of TDS records the MF B_u component of the SCM, whereas the other four channels record monopole or dipole potential voltages.

The search for magnetic signatures near the plasma frequency (typically between 50 and 100 kHz) in TDS bursts has been unsuccessful so far except for a few events that were found on 27 and 28 May 2020, when PSP was in its fifth encounter and at 0.37 AU from the Sun.

Out of the 170 bursts that were recorded on those 2 days, 25 show a statistically significant increase in spectral power density at the plasma frequency in both electric and magnetic fields. Figure 7 shows a strong event, which took place on May 27th at 18:45:24 UT. The electric field exhibits a distinctive coherent wave similar to what has been observed before in the solar wind by WIND, STEREO, and other spacecraft (Krafft et al., 2014). The peak frequency for that event is 64.8 kHz; this value is consistent with the plasma frequency of 63 kHz as inferred from the electron density by quasi-thermal noise spectroscopy (Moncuquet et al., 2020), given the uncertainty of the latter frequency estimate.

Interestingly, the magnetic field also shows evidence for a weak but significant excess of spectral power at the same plasma frequency, which suggests that PSP is very close to the source region of the type III radio burst or that the beam is fast (Malaspina et al., 2011).

The waveform of the associated wave is mostly hidden in the high level of interference noise. However, when we apply a narrow bandpass filter i.e., centered on the plasma frequency, a modulated wave pattern emerges, see Figure 7c. The connection between the electric and magnetic fields is further attested by the cross-coherence, which exhibits a highly significant peak at the plasma frequency. The phase difference between electric and magnetic fields slowly drifts in time, so that the peak value in the cross-coherence remains more modest than what visual inspections would suggest.

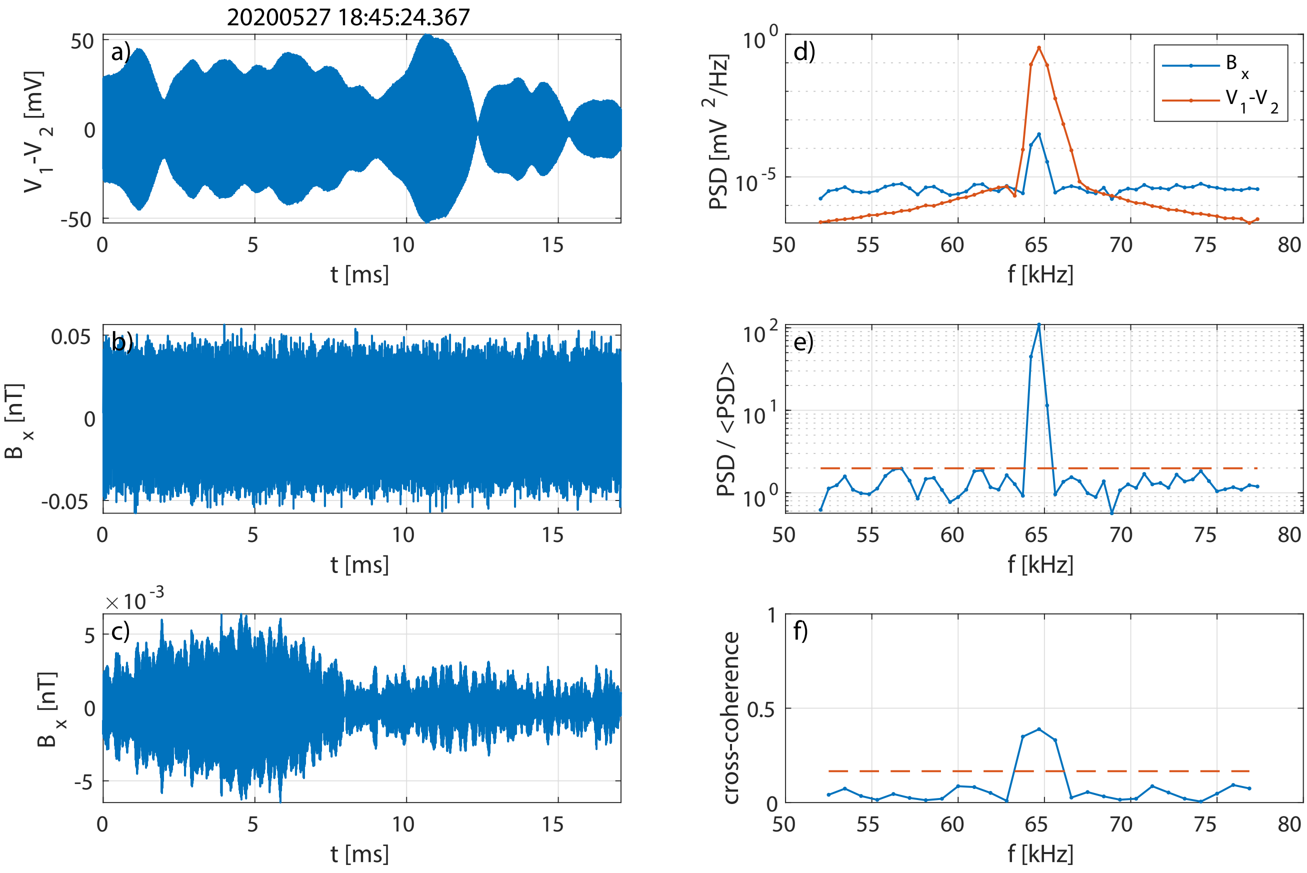

Figure 7. Example of a typical Langmuir wave event occurring on 27 May 2020 at 18:45:24 UT, with: (a) the dipolar electric potential, showing a large-amplitude quasi-monochromatic wave; (b) the waveform observed by the search coil magnetometer, which is dominated by interference noise from the spacecraft; (c) the same waveform, after bandpass filtering around the plasma frequency; (d) the power spectral density of the raw waveforms; (e) the power spectral density of the magnetic field, divided by the median value of that day - this is the quantity we use to detect the presence of spectral peaks associated with wave activity only - (f) the cross coherence between B_u and $V_1 - V_2$. On the last two plots the dashed line refers to the 99% confidence interval. We express the electric field in mV to avoid introducing uncertainties associated with the effective length of the antennas.

Several studies (Bale et al., 1996; Henri et al., 2009) have shown that the spectral peak of the electric field actually consists of two (sometimes partly overlapping) peaks. These peaks could be due to an incident wave and a wave that is reflected by density fluctuations (Krasnoselskikh et al., 2011), or to a three-wave interaction (Bale et al., 1996). Here we observe the same pattern. However, only one of the two peaks has a distinctive magnetic counterpart. While this could imply that one of the waves does not have a magnetic signature, a simpler explanation involves observational bias, with the weakest of the two peaks that are hidden in the noise level.

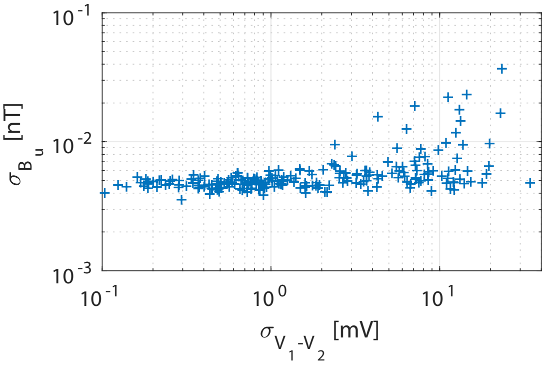

Figure 8. Comparison of the amplitude of the electric and magnetic waves. These amplitudes are estimated from the spectral peaks. The magnetic signal saturates around 5 pT because of the noise level. Only events for which σ_{B_u} significantly exceed that noise floor show a magnetic signature.

The challenge we are facing with these measurements is the weak magnetic signature relative to the level of interference noise. Figure 8 shows that the wave amplitude of the magnetic signature tends to increase with that of the electric field, once the former exceeds the instrumental noise level. No strict proportionality is expected since the ratio *B*/*E* depends on the polarization.

An alternative cause for these magnetic signatures could be interference by stray electric fields, most likely via the SCM. Although the sensitive parts of the SCM are shielded (see Sec. 3) and although various interference tests were performed prior to integration, the contribution of these interferences cannot be completely excluded, given the large amplitudes of the electric fields. The strongest evidence against such an effect comes from the lack of correlation between the amplitude of the electric and magnetic fields when one considers all Langmuir wave bursts. On several occasions, we saw bursts that had a larger electric field than the ones observed on 27-28 May 2020 and yet had no magnetic signature. This strongly supports the idea that the magnetic signature we observe on 27-28 May 2020 is related to specific plasma conditions and is not due to interference.

Recent results by Larosa et al. (2022), who combine simulations and energetic particle measurements from IS⊙IS show that all these features are consistent with the generation of slow extraordinary waves by large fluctuations in the electron density. These fluctuations affect the local refractive index and increases the B/E ratio. The beam energy is estimated to be between 1 and 3 keV so the proximity of the electron beam is likely to be the primary reason for which the magnetic component of the slow electromagnetic wave is observed for this particular event.

8. Example: Magnetic Signature of Dust Impacts

The impact of dust grains on spacecraft has been shown to produce short impulse-like perturbations of the electric field, which have received considerable attention (Zaslavsky, 2015). On PSP, these impulses typically last for a few tens of μsec and are best observed in the waveforms of the spacecraft potential as recorded by the TDS (Bale et al., 2016). The study of these impacts is motivated by the understanding of the dust distribution in the inner heliosphere, which has been shown to be complex and highly variable (Malaspina et al., 2020; Page et al., 2020; Pusack et al., 2021; Szalay et al., 2020, 2021).

Each impulse can be decomposed into distinct phases in the evolution of the spacecraft potential (Mann et al., 2019), which correspond, respectively, to the dust impact, the rapid emission of a cloud of electrons, followed by a slower escape of ions, and finally relaxation of the potential. While this global picture is widely accepted, the details of the response exhibit considerable variability.

So far, most dust impact studies had been based on the spacecraft potential only. The Wide Field Imager for Parker Solar Probe (WISPR) on PSP (Howard et al., 2019) has revealed the occasional impact of large dust grains with sizes of the order of 1 mm; these so-called impactors generate debris that floats around the spacecraft, reflect sunlight, and are visible when they cross the field of view of WISPR (Malaspina et al., 2022). These impactors generate large voltage swings that can last for many seconds.

Here we focus on smaller dust particles, whose size is of the order of 1 μm and below. These particles are much more numerous, and we report on the first observation of their magnetic signature. No such signatures had been reported before in the solar wind because they are weak, and high-frequency magnetic waveforms are rarely available. These results will be detailed in a forthcoming publication.

Figure 9 shows a typical example of a dust impact as recorded by the TDS, which provides burst waveforms sampled at 1.92 MHz. The upper plot (a) shows the MF B_u component, with no apparent event because the waveform is heavily polluted by interferences from the spacecraft and from the heater of the nearby MAG fluxgate magnetometer. Fortunately, since most interferences occur at frequencies that are stable in time, they can be strongly reduced by using the SVD method to separate coherent from incoherent fluctuations (Dudok de Wit, 1995). We apply the SVD to ensembles of several hundreds of waveforms and discard the components that have the largest singular values, which capture coherent interferences only. This method provides better results than Fourier filtering in which each of the spectral lines associated with interferences is removed manually.

The filtered waveform as shown in Figure 9b is approximately 20 dB below the noise level, and now clearly reveals a spike in the magnetic field. This spike occurs a few microseconds after the impact time seen in the differential potential $V_1 - V_2$ (Figure 9c) and in the potential V_5 recorded by the antenna that is located on the boom, next to the SCM.

The event shown in Figure 9 is a relatively weak one. Some are at least one order of magnitude larger. Figure 10 compares their peak magnetic signature with that of $|V_5|$, showing that only dust impacts with a large change in the electric potential have a magnetic signature. This plot suggests that all impacts have a magnetic signature, but that most of these remain hidden in the noise level.

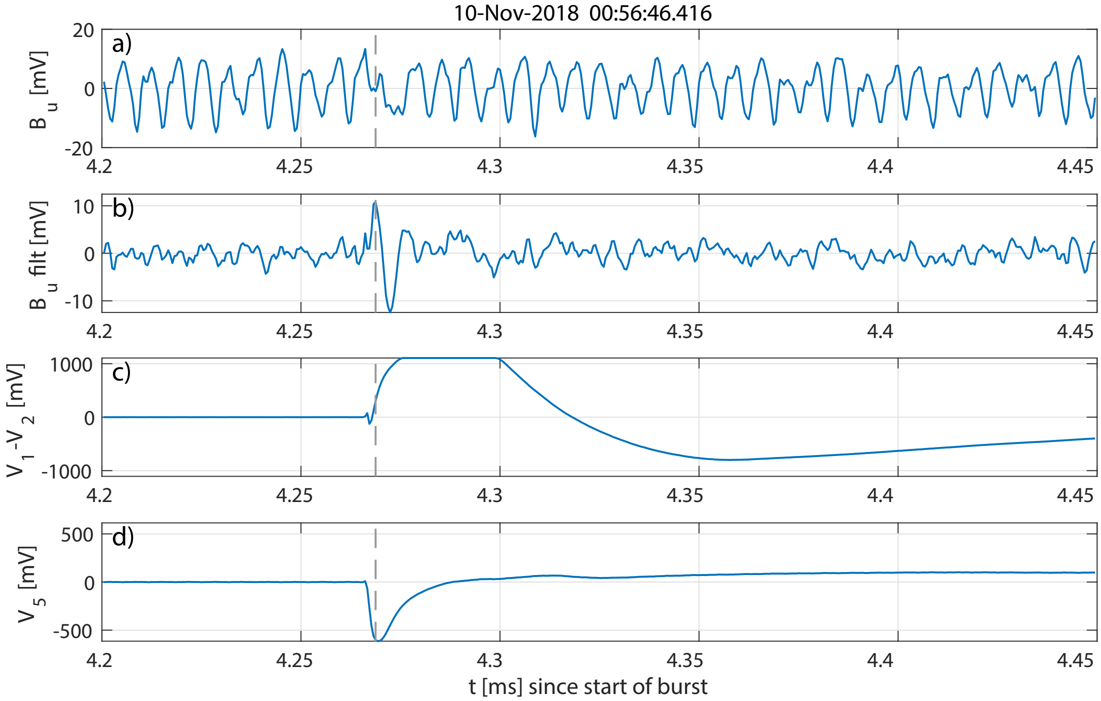

Figure 9. Example of a dust impact with magnetic signature, observed on 10 November 2018, showing: (a) the raw output from the search coil magnetometer (SCM), (b) the same output after removal of spacecraft interference, (c) the potential difference $V_1 - V_2$ (which saturates), and (d) the potential V_5 measured near the SCM. The dashed line is centered on the spike in the magnetic field.

As with the observation of intense Langmuir waves, one may wonder whether the impulses we see cannot be ascribed to the pick up of stray electric fields. This question has already been addressed in Section 7. Additional evidence against such an effect comes here from Figure 10, which shows that large spikes in the electric field do not necessarily have their magnetic counterpart.

Out of the 2128 waveforms recorded by TDS between launch and 2 May 2021, and with a dust impact, only 4% have an unambiguous magnetic signature. This fraction increases to 21% if we consider “large” dust impacts only, that is, those who could potentially have a magnetic signature, with a peak value of $|V_5|$ that exceeds 100 mV.

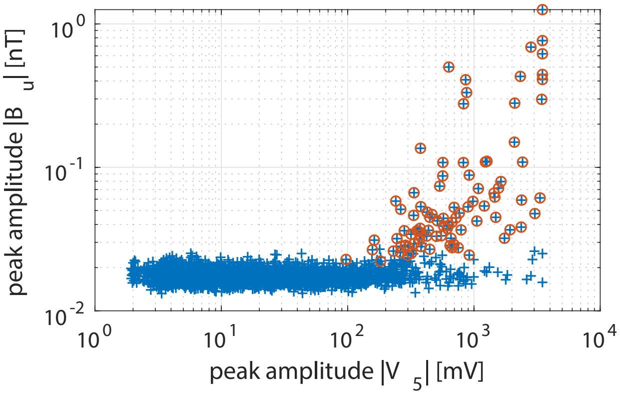

Figure 10. Comparison of the peak amplitude of $|B_u|$ versus the peak amplitude of $|V_5|$ for all 2128 dust impacts. Dust impacts with a well-identified magnetic signature are circled.

Previous studies (Malaspina et al., 2020; Pusack et al., 2021; Szalay et al., 2020, 2021) have shown that the dust count rate varies considerably with the distance to the Sun, but also the relative motion and orientation of the spacecraft. This rate is highest during the encounter phase. Figure 11 shows the distribution of bursts recorded by TDS versus the angular position of the spacecraft in heliocentric inertial coordinates. Here we have arbitrarily set the perihelion at 0°; the inbound leg corresponds to negative angles. The distribution of all impacts is strongly affected by the instrument observation strategy and should not be interpreted. The same figure, however, shows the fraction of impacts with magnetic signature relative to the total number of large impacts. The key result here is the absence of a significant angular (or radial) variation of this ratio, at a 5% level. From this, we conclude that the probability of observing a magnetic signature for a large impact depends on the intrinsic characteristics of the impact only, and not on the location of the spacecraft in the inner heliosphere, or on its relative motion.

A characteristic feature of all magnetic signatures is their occurrence during the initial phase only of the dust impact, that is, during the electron escape phase, which lasts for approximately 10 μsec. The ion escape phase takes

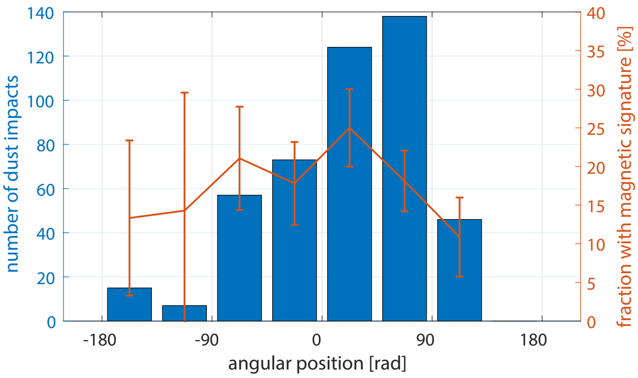

Figure 11. Angular distribution of dust impacts. The angle refers to the orbital position in heliocentric inertial coordinates: the perihelion is at 0° and negative angles correspond to the inbound part of the orbit. The full histogram expresses the total number of dust counts between launch and 2 May 2021. The red curve expressed the fractional amount of magnetic signatures versus "large" dust impacts.

much longer and the magnetic perturbation associated with the local increase in plasma pressure, if any, is likely to be far too weak to be observed.

By comparing the response of the dust impact on the different electric field antennas one can estimate where approximately the particle hit the spacecraft (Malaspina et al., 2020). If we assume that the recorded magnetic signature is associated with the current that is driven by the expanding cloud of electrons then we expect a stronger one-to-one relation between the magnitude of the electric and magnetic responses when these are measured close to each other. To check this we compare the peak value in $|B_u|$ with that of the other recorded waveforms ($|V_1 - V_2|$, $|V_2|$, $|V_3 - V_4|$ and $|V_5|$). These peak values span almost two orders of magnitude, so we use Spearman's rank correlation as a measure of similarity. We exclude peak amplitudes that are below the noise level, that is, $|B_u| < 0.025$ [nT], or have no significant signature at the time of the dust impact. The value of the correlation is low for all antennas, with values that are below 0.15. The only exception occurs for the V_5 antenna that is located next to the SCM. While these differences in the correlation may be partly explained by the frequent saturation of the former three types of waveforms, they nevertheless suggest that there is a closer one-to-one relationship between electric and magnetic signatures when the impact occurs near the search-coil.

Finally, let us mention that magnetic signatures are also observed for large impactors. Their magnetic signature occurs during the early expansion phase and lasts for several ms (Malaspina et al., 2022).

9. Conclusions and Lessons Learned

After more than 3 years of operation, the SCM onboard Parker Solar Probe has proven its ability to meet its scientific objectives, with the characterization of the different types of waves, such as whistler and ion cyclotron waves. Although most of the whistler waves are quasi-parallel, a few percent of them are found to be oblique. This preliminary result suggests that whistler waves may play an important role in scattering Strahl suprathermal electrons into a halo population. There were some surprises in the high-frequency range of the instrument, with the observation of the magnetic signature of escaping electrons during dust impacts and the observation of the magnetic component of the slow extraordinary mode during type III radio bursts.

Besides usual data products such as waveforms (both continuous survey and high cadence bursts), auto-spectra, and cross-spectra, FIELDS also provides a merged data set that combines fluxgate and search-coil observations in one single and seamless waveform (Bowen, Bale, et al., 2020).

The SCM is operating nominally apart from a sudden drop in sensitivity at low frequency, which occurred between 3 and 4 March 2019, and has since affected the response of the LF B_u channel. This anomaly is attributed to thermal stresses in the preamplifier and the response has been stable since. Unfortunately, the absence of one out of three components of the magnetic field has hampered our capacity to estimate properties such as wave polarization after the first solar encounter in November 2018.

The on-board calibration of the SCM and its cross-calibration with the MAG fluxgate magnetometer confirm the stability of the performance of the instrument and the good agreement with pre-flight calibrations.

The main lesson learned from these 3 years of operation is the relatively weaker than the expected amplitude of the magnetic field fluctuations, which means that higher instrument gains would have been possible without the risk of saturating the instrument. Currently, the largest measurable amplitude in the LF range is 185 nT in high gain mode and 15 times higher in low gain mode. These values could easily have been reduced by one order of magnitude, thereby allowing greater confidence in the electrostatic nature of waves that are often observed in the electric field but have no detectable counterpart or no signature at all in the magnetic field. A higher gain of the SCM, however, only makes sense with better electromagnetic cleanliness. With Parker Solar Probe, the omnipresent signature of reaction wheels is a major source of electromagnetic pollution between a few Hz, and approximately 100 Hz.

From a more technical perspective, having the same clock for both MAG and SCM has considerably helped compare their waveforms and develop a merged data product. Finally, and not least, a full system-level calibration of both MAG and SCM would have greatly helped in understanding and correcting the small discrepancies that remain between the two instruments. Similarly, a phase calibration with the electric field antennas would have been valuable in helping to unambiguously identify electromagnetic waves. Although intercalibrations can be partly performed in flight with specific waves (e.g., whistlers) we cannot stress enough the importance of performing them on the ground.

Data Availability Statement

Level 2 and 3 data from the FIELDS instrument suite are publicly available from the FIELDS website (https://fields.ssl.berkeley.edu/data/) and from NASA's Space Physics Data Facility (SPDF, https://cdaweb.gsfc.nasa.gov), which also covers datasets from the other instrument suites. The level 3 merged magnetic field data product is further described in (Bowen, Bale, et al., 2020). A full description of the DFB data products is available in (Malaspina et al., 2016). A large subset of SCM and MAG data is available from the French National Data Centre for Space Plasmas (CDPP, http://cdpp.eu), including further descriptions of these instruments, and in particular the Noise Equivalent Magnetic Induction (NEMI) of the SCM. The Parker Solar Probe Science Gateway (https://sppgway.jhuapl.edu/encounters) provides additional information on each encounter, such as the distance from the Sun, etc. PSP/FIELDS data are released a few months after each encounter. The present data are based on release 8 (28 June 2021). More information on the data release history can be found at the FIELDS website (https://fields.ssl.berkeley.edu/data/). All publications which use FIELDS data should cite the FIELDS instrument paper (Bale et al., 2016) and include the following statement in the acknowledgements: "The FIELDS experiment on the Parker Solar Probe spacecraft was designed and developed under NASA contract NNN06AA01 C". Those using, in addition, SCM data should cite (Jannet et al., 2021) and include the statement: "The development, processing, and analysis of SCM data are funded by CNES."

Acknowledgments

The SCM team is grateful to the FIELDS and RPW teams. We particularly thank Patrice Fergeau, as well as Jean-Yves Prado, Kader Amsif, and François Gonzalez from the French Space Agency (CNES) for their continuing support. The FIELDS experiment on the Parker Solar Probe spacecraft was designed and developed under NASA contract NNN06AA01 C. Parker Solar Probe was designed, built, and is now operated by the Johns Hopkins Applied Physics Laboratory as part of NASA's Living with a Star (LWS) program (contract NNN06AA01 C). Support from the LWS management and technical team has played a critical role in the success of the Parker Solar Probe mission. The development, processing and analysis of SCM data is funded by CNES. VK and OVA were supported by NASA Grant 80NSSC20K0697 and 80NSSC21K1770; OVA was partially supported by NSF Grant Nos. 1914670 and NASA Living with a Star (LWS) program (contract 80NSSC20K0218), 80NNSC19K0848, and 80NSSC22K0417. All the data used in this work are publicly available from the websites that are listed in the Data Availability Statement.

References

Agapitov, O. V., Artemyev, A. V., Mourenas, D., Krasnoselskikh, V., Bonnell, J., Contel, O. L., et al. (2014). The quasi-electrostatic mode of chorus waves and electron nonlinear acceleration. *Journal of Geophysical Research: Space Physics*, *119*(3), 1606–1626. https://doi.org/10.1002/2013JA019223

Agapitov, O. V., Dudok de Wit, T., Mozer, F. S., Bonnell, J. W., Drake, J. F., Malaspina, D., & Wygant, J. R. (2020). Sunward-propagating whistler waves collocated with localized magnetic field holes in the solar wind: Parker solar probe observations at 35.7 $R_\odot$ radii. *The Astrophysical Journal Letters*, *891*(1), L20. https://doi.org/10.3847/2041-8213/ab799c

Alexandrova, O., Jagarlamudi, V. K., Hellinger, P., Maksimovic, M., Shprits, Y., & Mangeney, A. (2021). Spectrum of kinetic plasma turbulence at 0.3-0.9 astronomical units from the Sun. *Physical Review E*, *103*(6), 063202. https://doi.org/10.1103/PhysRevE.103.063202

Alexandrova, O., Lacombe, C., Mangeney, A., Grappin, R., & Maksimovic, M. (2012). Solar wind turbulent spectrum at plasma kinetic scales. *The Astrophysical Journal*, *760*(2), 121. https://doi.org/10.1088/0004-637X/760/2/121

Alexandrova, O., Saur, J., Lacombe, C., Mangeney, A., Mitchell, J., Schwartz, S. J., & Robert, P. (2009). Universality of solar-wind turbulent spectrum from MHD to electron scales. *Physical Review Letters*, *103*(16), 165003. https://doi.org/10.1103/PhysRevLett.103.165003

Artemyev, A., Agapitov, O., Mourenas, D., Krasnoselskikh, V., Shastun, V., & Mozer, F. (2016). Oblique whistler-mode waves in the Earth's inner magnetosphere: Energy distribution, origins, and role in radiation belt dynamics. *Space Science Reviews*, *200*(1–4), 261–355. https://doi.org/10.1007/s11214-016-0252-5

Bale, S. D., Badman, S. T., Bonnell, J. W., Bowen, T. A., Burgess, D., Case, A. W., & Wygant, J. R. (2019). Highly structured slow solar wind emerging from an equatorial coronal hole. *Nature*, *576*, 237–242. https://doi.org/10.1038/s41586-019-1818-7

Bale, S. D., Burgess, D., Kellogg, P. J., Goetz, K., Howard, R. L., & Monson, S. J. (1996). Phase coupling in Langmuir wave packets: Possible evidence of three-wave interactions in the upstream solar wind. *Geophysical Research Letters*, *23*, 109–112. https://doi.org/10.1029/95GL03595

Bale, S. D., Goetz, K., Harvey, P. R., Turin, P., Bonnell, J. W., Dudok de Wit, T., & Wygant, J. R. (2016). The FIELDS instrument suite for solar probe plus. *Space Science Reviews*, *204*(49), 1–34. https://doi.org/10.1007/s11214-016-0244-5

Bale, S. D., Kellogg, P. J., Goetz, K., & Monson, S. J. (1998). Transverse z-mode waves in the terrestrial electron foreshock. *Geophysical Research Letters*, *25*(1), 9–12. https://doi.org/10.1029/97GL03493

Bowen, T. A., Bale, S. D., Bandyopadhyay, R., Bonnell, J. W., Case, A., Chasapis, A., & Whittlesey, P. (2021). Kinetic-scale turbulence in the Venusian magnetosheath. *Geophysical Research Letters*, *48*(2), e90783. https://doi.org/10.1029/2020GL090783

Bowen, T. A., Mallet, A., Huang, J., Klein, K. G., Malaspina, D. M., Stevens, M., & Whittlesey, P. (2020). Ion-scale electromagnetic waves in the inner heliosphere. *The Astrophysical Journal - Supplement Series*, *246*(2), 66. https://doi.org/10.3847/1538-4365/ab6c65

Bruno, R., & Carbone, V. (2013). The solar wind as a turbulence laboratory. *Living Reviews in Solar Physics*, *2*, 4. https://doi.org/10.12942/lrsp-2013-2

Cattell, C. A., Short, B., Breneman, A. W., & Grul, P. (2020). Narrowband large amplitude whistler-mode waves in the solar wind and their association with electrons: STEREO waveform capture observations. *The Astrophysical Journal*, *897*(2), 126. https://doi.org/10.3847/1538-4357/ab961f

Cattell, C., Short, B., Breneman, A., Halekas, J., Whittesley, P., Larson, D., & Pulupa, M. (2021). Narrowband oblique whistler-mode waves: Comparing properties observed by Parker Solar Probe inside 0.2 AU and by STEREO at 1 AU. *Astronomy and Astrophysics*, *650*(A8). https://doi.org/10.1051/0004-6361/202039550

Chaston, C. C., Bonnell, J. W., Bale, S. D., Kasper, J. C., Pulupa, M., Dudok de Wit, T., & Malaspina, D. M. (2020). MHD mode composition in the inner heliosphere from the parker solar probe's first perihelion. *The Astrophysical Journal - Supplement Series*, *246*(2), 71. https://doi.org/10.3847/1538-4365/ab745c

Chhiber, R., Matthaeus, W. H., Bowen, T. A., & Bale, S. D. (2021). Subproton-scale intermittency in near-sun solar wind turbulence observed by the parker solar probe. *The Astrophysical Journal Letters*, *911*(1), L7. https://doi.org/10.3847/2041-8213/abf04e

Cornilleau-Wehrlin, N., Chanteur, G., Perraut, S., Rezeau, L., Robert, P., Roux, A., et al. (2003). First results obtained by the Cluster STAFF experiment. *Annales Geophysicae*, *21*, 437–456. https://doi.org/10.5194/angeo-21-437-2003

Drake, J. F., Agapitov, O., Swisdak, M., Badman, S. T., Bale, S. D., Horbury, T. S., & Velli, M. (2021). Switchbacks as signatures of magnetic flux ropes generated by interchange reconnection in the corona. *Astronomy and Astrophysics*, *650*. A2. https://doi.org/10.1051/0004-6361/202039432

Dudok de Wit, T. (1995). Enhancement of multichannel data in plasma physics by biorthogonal decomposition. *Plasma Physics and Controlled Fusion*, *37*, 117–135. https://doi.org/10.1088/0741-3335/37/2/005

Dudok de Wit, T., Krasnoselskikh, V. V., Bale, S. D., Bonnell, J. W., Bowen, T. A., Chen, C. H. K., et al. (2020). Switchbacks in the near-sun magnetic field: Long memory and impact on the turbulence cascade. *The Astrophysical Journal Supplement*, *246*(2), 39. https://doi.org/10.3847/1538-4365/ab5853

Farrell, W. M., MacDowall, R. J., Gruesbeck, J. R., Bale, S. D., & Kasper, J. C. (2020). Magnetic field dropouts at near-sun switchback boundaries: A superposed epoch analysis. *The Astrophysical Journal - Supplement Series*, *249*(2), 28. https://doi.org/10.3847/1538-4365/ab9eba

Fischer, D., Magnes, W., Hagen, C., Dors, I., Chutter, M. W., Needell, J., & Baumjohann, W. (2016). Optimized merging of search coil and fluxgate data for MMS. *Geoscientific Instrumentation, Methods and Data Systems*, *5*(2), 521–530. https://doi.org/10.5194/gi-5-521-2016

Fox, N. J., Velli, M. C., Bale, S. D., Decker, R., Driesman, A., Howard, R. A., et al. (2015). The solar probe plus mission: Humanity's first visit to our star. *Space Science and Review*, *204*, 1–42. https://doi.org/10.1007/s11214-015-0211-6

Freund, H. P., & Papadopoulos, K. (1980). Radiation from a localized Langmuir oscillation in a uniformly magnetized plasma. *Physics of Fluids*, *23*(8), 1546–1552. https://doi.org/10.1063/1.863166

Froment, C., Krasnoselskikh, V., Dudok de Wit, T., Agapitov, O., Fargette, N., Lavraud, B., et al. (2021). Direct evidence for magnetic reconnection at the boundaries of magnetic switchbacks with Parker Solar Probe. *Astronomy and Astrophysics*, *650*. A5. https://doi.org/10.1051/0004-6361/202039806

Gary, S. P., & Feldman, W. C. (1977). Solar wind heat flux regulation by the whistler instability. *Journal of Geophysical Research*, *82*(7), 1087. https://doi.org/10.1029/JA082i007p01087

Gary, S. P., & Li, H. (2000). Whistler heat flux instability at high Beta. *The Astrophysical Journal*, *529*(2), 1131–1135. https://doi.org/10.1086/308294

Gary, S. P., Scime, E. E., Phillips, J. L., & Feldman, W. C. (1994). The whistler heat flux instability: Threshold conditions in the solar wind. *Journal of Geophysical Research*, *99*(A12), 23391–23400. https://doi.org/10.1029/94JA02067

Ginzburg, V. L., & Zhelezniakov, V. V. (1958). On the possible mechanisms of sporadic solar radio emission (radiation in an isotropic plasma). *Soviet Astronomy*, *2*, 653.

Graham, G. A., Rae, I. J., Owen, C. J., Walsh, A. P., Arridge, C. S., Gilbert, L., & Waite, J. H. (2017). The evolution of solar wind strahl with heliospheric distance. *Journal of Geophysical Research*, *122*(4), 3858–3874. https://doi.org/10.1002/2016JA023656

Gurnett, D. A., & Frank, L. A. (1975). Electron plasma oscillations associated with type III radio emissions and solar electrons. *Solar Physics*, *45*(2), 477–493. https://doi.org/10.1007/BF00158464

Gurnett, D. A., Kurth, W. S., Kirchner, D. L., Hospodarsky, G. B., Averkamp, T. F., Zarka, P., et al. (2004). The Cassini radio and plasma wave investigation. *Space Science Reviews*, *114*, 395–463. https://doi.org/10.1007/s11214-004-1434-0

Halekas, J. S., Whittlesey, P., Larson, D. E., McGinnis, D., Maksimovic, M., Berthomier, M., et al. (2020). Electrons in the young solar wind: First results from the parker solar probe. *The Astrophysical Journal - Supplement Series*, *246*(2), 22. https://doi.org/10.3847/1538-4365/ab4cec

Hammond, C. M., Feldman, W. C., McComas, D. J., Phillips, J. L., & Forsyth, R. J. (1996). Variation of electron-strahl width in the high-speed solar wind: ULYSSES observations. *Astronomy and Astrophysics*, *316*, 350–354.

Henri, P., Briand, C., Mangeney, A., Bale, S. D., Califano, F., Goetz, K., & Kaiser, M. (2009). Evidence for wave coupling in type III emissions. *Journal of Geophysical Research*, *114*(A13), 3103. https://doi.org/10.1029/2008JA013738

Hollweg, J. V. (1982). Surface waves on solar wind tangential discontinuities. *Journal of Geophysical Research*, *87*(A10), 8065–8076. https://doi.org/10.1029/JA087iA10p08065

Horaites, K., Boldyrev, S., Krasheninnikov, S. I., Salem, C., Bale, S. D., & Pulupa, M. (2015). Self-similar theory of thermal conduction and application to the solar wind. *Physical Review Letters*, *114*(24), 245003. https://doi.org/10.1103/PhysRevLett.114.245003

Horbury, T. S., Woolley, T., Laker, R., Matteini, L., Eastwood, J., Bale, S. D., et al. (2020). Sharp alfvénic impulses in the near-sun solar wind. *The Astrophysical Journal - Supplement Series*, *246*(2), 45. https://doi.org/10.3847/1538-4365/ab5b15

Howard, R. A., Vourlidas, A., Bothmer, V., Colaninno, R. C., DeForest, C. E., Gallagher, B., et al. (2019). Near-Sun observations of an F-corona decrease and K-corona fine structure. *Nature*, *576*, 232–236. . https://doi.org/10.1038/s41586-019-1807-x

Huang, S. Y., Sahraoui, F., Andrés, N., Hadid, L. Z., Yuan, Z. G., He, J. S., et al. (2021). The ion transition range of solar wind turbulence in the inner heliosphere: Parker solar probe observations. *The Astrophysical Journal Letters*, *909*(1), L7. https://doi.org/10.3847/2041-8213/abdaaf

Jagarlamudi, V. K., Alexandrova, O., Berčič, L., Dudok de Wit, T., Krasnoselskikh, V., Maksimovic, M., & Štverák, Š. (2020). Whistler waves and electron properties in the inner heliosphere: Helios observations. *The Astrophysical Journal*, *897*(2), 118. https://doi.org/10.3847/1538-4357/ab94a1

Jagarlamudi, V. K., Dudok de Wit, T., Froment, C., Krasnoselskikh, V., Larosa, A., Bercic, L., et al. (2021). Whistler wave occurrence and the interaction with strahl electrons during the first encounter of Parker Solar Probe. *Astronomy and Astrophysics*, *650*(A9). https://doi.org/10.1051/0004-6361/202039808

Jannet, G., Dudok de Wit, T., Krasnoselskikh, V., Kretzschmar, M., Fergeau, P., Bergerard-Timofeeva, M., et al. (2021). Measurement of magnetic field fluctuations in the parker solar probe and solar orbiter missions. *Journal of Geophysical Research: Space Physics*, *126*(2), e2020JA028543. https://doi.org/10.1029/2020JA028543

Kajdič, P., Alexandrova, O., Maksimovic, M., Lacombe, C., & Fazakerley, A. N. (2016). Suprathermal electron strahl widths in the presence of narrow-band whistler waves in the solar wind. *The Astrophysical Journal*, *833*(2), 172. https://doi.org/10.3847/1538-4357/833/2/172

Kasper, J. C., Bale, S. D., Belcher, J. W., Berthomier, M., Case, A. W., Chandran, B. D. G., et al. (2019). Alfvénic velocity spikes and rotational flows in the near-Sun solar wind. *Nature*, *576*, 228–231. https://doi.org/10.1038/s41586-019-1813-z

Kellogg, P. J. (2003). Langmuir waves associated with collisionless shocks; a review. *Planetary and Space Science*, *51*(11), 681–691. https://doi.org/10.1016/j.pss.2003.05.001

Kellogg, P. J., Goetz, K., Monson, S. J., & Bale, S. D. (1999). Langmuir waves in a fluctuating solar wind. *Journal of Geophysical Research*, *104*, 17069–17078. https://doi.org/10.1029/1999JA900163

Khabarova, O., & Obridko, V. (2012). Puzzles of the interplanetary magnetic field in the inner heliosphere. *The Astrophysical Journal*, *761*(2), 82. https://doi.org/10.1088/0004-637X/761/2/82

Kim, E.-H., Cairns, I. H., & Johnson, J. R. (2013). Linear mode conversion of Langmuir/z-mode waves to radiation in plasmas with various magnetic field strength. *Physics of Plasmas*, *20*(12), 122103. https://doi.org/10.1063/1.4837515

Kiyani, K. H., Osman, K. T., & Chapman, S. C. (2015). Dissipation and heating in solar wind turbulence: From the macro to the micro and back again. *Philosophical Transactions of the Royal Society of London A: Mathematical, Physical and Engineering Sciences*, *373*(20140155). https://doi.org/10.1098/rsta.2014.0155

Krafft, C., Volokitin, A. S., Krasnoselskikh, V. V., & Dudok de Wit, T. (2014). Waveforms of Langmuir turbulence in inhomogeneous solar wind plasmas. *Journal of Geophysical Research: Space Physics*, *119*(12), 2014JA020329. https://doi.org/10.1002/2014JA020329

Krasnoselskikh, V. V., Dudok de Wit, T., & Bale, S. D. (2011). Determining the wavelength of Langmuir wave packets at the Earth's bow shock. *Annales Geophysicae*, *29*, 613–617. https://doi.org/10.5194/angeo-29-613-2011

Krasnoselskikh, V., Larosa, A., Agapitov, O., Dudok de Wit, T., Moncuquet, M., Mozer, F. S., et al. (2020). Localized magnetic-field structures and their boundaries in the near-sun solar wind from parker solar probe measurements. *The Astrophysical Journal*, *893*(2), 93. https://doi.org/10.3847/1538-4357/ab7f2d

Krasnoselskikh, V., Voshchepynets, A., & Maksimovic, M. (2019). On the efficiency of the linear-mode conversion for generation of solar type III radio bursts. *The Astrophysical Journal*, *879*(1), 51. https://doi.org/10.3847/1538-4357/ab22bf

Krauss-Varban, D. (1989). Beam instability of the Z mode in the solar wind. *Journal of Geophysical Research*, *94*(A4), 3527–3534. https://doi.org/10.1029/JA094iA04p03527

Lacombe, C., Alexandrova, O., Matteini, L., Santolík, O., Cornilleau-Wehrlin, N., Mangeney, A., & Maksimovic, M. (2014). Whistler mode waves and the electron heat flux in the solar wind: Cluster observations. *The Astrophysical Journal*, *796*, 5. https://doi.org/10.1088/0004-637X/796/1/5

Landi, S., Matteini, L., & Pantellini, F. (2014). Electron heat flux in the solar wind: Are we observing the collisional limit in the 1 AU data? *The Astrophysical Journal Letters*, *790*(1), L12. https://doi.org/10.1088/2041-8205/790/1/L12

Larosa, A., Dudok de Wit, T., Krasnoselskikh, V., Bale, S. D., Agapitov, O., Bonnell, J., et al. (2022). Langmuir-Slow extraordinary mode magnetic signature observations with parker solar probe. *The Astrophysical Journal*, *927*(1), 95. https://doi.org/10.3847/1538-4357/ac4e85

Larosa, A., Krasnoselskikh, V., Dudok de Wit, T., Agapitov, O., Froment, C., Jagarlamudi, V. K., et al. (2020). Switchbacks: Statistical properties and deviations from alfvénicity. *Astronomy and Astrophysics*,. https://doi.org/10.1051/0004-6361/202039442

Le Contel, O., Leroy, P., Roux, A., Coillot, C., Alison, D., Bouabdellah, A., et al. (2014). The search-coil magnetometer for MMS. *Space Science Review*, *199*(1–4), 257–282. https://doi.org/10.1007/s11214-014-0096-9

Lin, R. P., Potter, D. W., Gurnett, D. A., & Scarf, F. L. (1981). Energetic electrons and plasma waves associated with a solar type III radio burst. *The Astrophysical Journal*, *251*, 364–373. https://doi.org/10.1086/159471

Maksimovic, M., Bale, S. D., Chust, T., Khotyaintsev, Y., Krasnoselskikh, V., Kretzschmar, M., et al. (2020). The solar orbiter radio and plasma waves (RPW) instrument. *Astronomy and Astrophysics*, *642*, A12. https://doi.org/10.1051/0004-6361/201936214

Maksimovic, M., Zouganelis, I., Chaufray, J. Y., Issautier, K., Scime, E. E., Littleton, J. E., et al. (2005). Radial evolution of the electron distribution functions in the fast solar wind between 0.3 and 1.5 au. *Journal of Geophysical Research*, *110*(A9), A09104. https://doi.org/10.1029/2005JA011119

Malaspina, D. M., Cairns, I. H., & Ergun, R. E. (2011). Dependence of Langmuir wave polarization on electron beam speed in type III solar radio bursts. *Geophysical Research Letters*, *38*(13), L13101. https://doi.org/10.1029/2011GL047642

Malaspina, D. M., Ergun, R. E., Bolton, M., Kien, M., Summers, D., Stevens, K., et al. (2016). The digital fields board for the fields instrument suite on the solar probe plus mission: Analog and digital signal processing. *Journal of Geophysical Research: Space Physics*, *121*(6), 5088–5096. https://doi.org/10.1002/2016JA022344

Malaspina, D. M., Stenborg, G., Mehoke, D., Al-Ghazwi, A., Shen, M. M., Hsu, H.-W., et al. (2022). Clouds of spacecraft debris liberated by hypervelocity dust impacts on parker solar probe. *The Astrophysical Journal*, *925*(1), 27. https://doi.org/10.3847/1538-4357/ac3bbb

Malaspina, D. M., Szalay, J. R., Pokorný, P., Page, B., Bale, S. D., Bonnell, J. W., et al. (2020). In situ observations of interplanetary dust variability in the inner heliosphere. *The Astrophysical Journal*, *892*(2), 115. https://doi.org/10.3847/1538-4357/ab799b

Mann, I., Nouzák, L., Vaverka, J., Antonsen, T., Fredriksen, Å., Issautier, K., et al. (2019). Dust observations with antenna measurements and its prospects for observations with parker solar probe and solar orbiter. *Annales Geophysicae*, *37*(6), 1121–1140. https://doi.org/10.5194/angeo-37-1121-2019

Marsch, E. (2006). Kinetic physics of the solar corona and solar wind. *Living Reviews in Solar Physics*, *3*(1), 1. https://doi.org/10.12942/lrsp-2006-1

McComas, D. J., Christian, E. R., Cohen, C. M. S., Cummings, A. C., Davis, A. J., Desai, M. I., et al. (2019). Probing the energetic particle environment near the Sun. *Nature*, *576*, 223–227. https://doi.org/10.1038/s41586-019-1811-1

Moncuquet, M., Meyer-Vernet, N., Issautier, K., Pulupa, M., Bonnell, J. W., Bale, S. D., et al. (2020). First in situ measurements of electron density and temperature from quasi-thermal noise spectroscopy with parker solar probe/FIELDS. *The Astrophysical Journal - Supplement Series*, *246*(2), 44. https://doi.org/10.3847/1538-4365/ab5a84

Mozer, F. S., Agapitov, O. V., Bale, S. D., Bonnell, J. W., Case, T., Chaston, C. C., et al. (2020). Switchbacks in the solar magnetic field: Their evolution, their content, and their effects on the plasma. *The Astrophysical Journal - Supplement Series*, *246*(2), 68. https://doi.org/10.3847/1538-4365/ab7196

Neubauer, F. M., Beinroth, H. J., Barnstorf, H., & Dehmel, G. (1977). Initial results from the Helios-1 search-coil magnetometer experiment. *Journal of Geophysics/Zeitschrift für Geophysik*, *42*(6), 599–614.

Ogilvie, K. W., & Scudder, J. D. (1978). The radial gradients and collisional properties of solar wind electrons. *Journal of Geophysical Research*, *83*(A8), 3776–3782. https://doi.org/10.1029/JA083iA08p03776

Page, B., Bale, S. D., Bonnell, J. W., Goetz, K., Goodrich, K., Harvey, P. R., et al. (2020). Examining dust directionality with the parker solar probe FIELDS instrument. *The Astrophysical Journal - Supplement Series*, *246*(2), 51. https://doi.org/10.3847/1538-4365/ab5f6a

Papadopoulos, K., & Freund, H. P. (1978). Solitons and second harmonic radiation in type III bursts. *Geophysical Research Letters*, *5*(10), 881–884. https://doi.org/10.1029/GL005i010p00881

Papadopoulos, K., & Freund, H. P. (1979). Collective radio emission from plasmas. *Space Science Reviews*, *24*(4), 511–566. https://doi.org/10.1007/BF00172213

Parrot, M., Benoist, D., Berthelier, J. J., Błęcki, J., Chapuis, Y., Colin, F., et al. (2006). The magnetic field experiment IMSC and its data processing onboard DEMETER: Scientific objectives, description and first results. *Planetary and Space Science*, *54*, 441–455. https://doi.org/10.1016/j.pss.2005.10.015

Pfaff, R. F., Borovsky, J. E., & Young, D. T. (1998). Measurement Techniques in Space Plasmas – Fields (Vol. *103*). *American Geophysical Union*.

Pierrard, V., & Voitenko, Y. (2010). Velocity distributions and Proton beam production in the solar wind. In M.Maksimovic, K.Issautier, N.Meyer-Vernet, M.Moncuquet, & F.Pantellini (Eds.), Presented at the *Twelfth international solar wind conference*. (Vol. 1216, pp. 102–105). https://doi.org/10.1063/1.3395812

Pilipp, W. G., Miggenrieder, H., Montgomery, M. D., Mühlhäuser, K. H., Rosenbauer, H., & Schwenn, R. (1987). Characteristics of electron velocity distribution functions in the solar wind derived from the helios plasma experiment. *Journal of Geophysical Research*, *92*(A2), 1075–1092. https://doi.org/10.1029/JA092iA02p01075

Pulupa, M., Bale, S. D., Bonnell, J. W., Bowen, T. A., Carruth, N., Goetz, K., et al. (2017). The solar probe plus radio frequency spectrometer: Measurement requirements, analog design, and digital signal processing. *Journal of Geophysical Research: Space Physics*, *122*(3), 2836–2854. https://doi.org/10.1002/2016JA023345

Pusack, A., Malaspina, D. M., Szalay, J. R., Bale, S. D., Goetz, K., MacDowall, R. J., & Pulupa, M. (2021). Dust directionality and an anomalous interplanetary dust population detected by the parker solar probe. *The Planetary Science Journal*, *2*(5), 186. https://doi.org/10.3847/PSJ/ac0bb9

Roberg-Clark, G. T., Agapitov, O., Drake, J. F., & Swisdak, M. (2019). Scattering of energetic electrons by heat-flux-driven whistlers in flares. *The Astrophysical Journal*, *887*, 190. https://doi.org/10.3847/1538-4357/ab5114

Roberg-Clark, G. T., Drake, J. F., Swisdak, M., & Reynolds, C. S. (2018). Wave generation and heat flux suppression in astrophysical plasma systems. *The Astrophysical Journal*, *867*, 154. https://doi.org/10.3847/1538-4357/aae393

Rosenbauer, H., Schwenn, R., Marsch, E., Meyer, B., Miggenrieder, H., Montgomery, M. D., et al. (1977). A survey on initial results of the HELIOS plasma experiment. *Journal of Geophysics Zeitschrift Geophysik*, *42*(6), 561–580.

Sahraoui, F., Goldstein, M. L., Robert, P., & Khotyaintsev, Y. V. (2009). Evidence of a cascade and dissipation of solar-wind turbulence at the electron gyroscale. *Physical Review Letters*, *102*(23), 231102. https://doi.org/10.1103/PhysRevLett.102.231102

Sahraoui, F., Huang, S. Y., Belmont, G., Goldstein, M. L., Rétino, A., Robert, P., & De Patoul, J. (2013). Scaling of the electron dissipation range of solar wind turbulence. *The Astrophysical Journal*, *777*, 15. https://doi.org/10.1088/0004-637X/777/1/15

Santolík, O., Parrot, M., & Lefeuvre, F. (2003). Singular value decomposition methods for wave propagation analysis. *Radio Science*, *38*(1). https://doi.org/10.1029/2000RS002523

Scarf, F. L., Fredricks, R. W., Frank, L. A., & Neugebauer, M. (1971). Nonthermal electrons and high-frequency waves in the upstream solar wind, 1. Observations. *Journal of Geophysical Research*, *76*(22), 5162–5171. https://doi.org/10.1029/ja076i022p05162

Scarf, F. L., Fredricks, R. W., Green, I. M., & Neugebauer, M. (1970). OGO 5 observations of quasi-trapped electromagnetic waves in the solar wind. *Journal of Geophysical Research*, *75*(19), 3735. https://doi.org/10.1029/JA075i019p03735

Scime, E. E., Bame, S. J., Feldman, W. C., Gary, S. P., Phillips, J. L., & Balogh, A. (1994). Regulation of the solar wind electron heat flux from 1 to 5 AU: Ulysses observations. *Journal of Geophysical Research*, *99*(A12), 23401–23410. https://doi.org/10.1029/94JA02068

Séran, H. C., & Fergeau, P. (2005). An optimized low-frequency three-axis search coil magnetometer for space research. *Review of Scientific Instruments*, *76*(4), 044502. https://doi.org/10.1063/1.1884026

Spitzer, L., & Härm, R. (1953). Transport phenomena in a completely ionized gas. *Physical Review*, *89*(5), 977–981. https://doi.org/10.1103/PhysRev.89.977

Stansby, D., Horbury, T. S., Chen, C. H. K., & Matteini, L. (2016). Experimental determination of whistler wave Dispersion relation in the solar wind. *The Astrophysical Journal Letters*, *829*, L16. https://doi.org/10.3847/2041-8205/829/1/L16

Štverák, Š., Maksimovic, M., Trávníček, P. M., Marsch, E., Fazakerley, A. N., & Scime, E. E. (2009). Radial evolution of nonthermal electron populations in the low-latitude solar wind: Helios, Cluster, and Ulysses Observations. *Journal of Geophysical Research*, *114*(A5), A05104. https://doi.org/10.1029/2008JA013883

Szalay, J. R., Pokorný, P., Bale, S. D., Christian, E. R., Goetz, K., Goodrich, K., et al. (2020). The near-sun dust environment: Initial observations from parker solar probe. *The Astrophysical Journal Supplement*, *246*(2), 27. https://doi.org/10.3847/1538-4365/ab50c1

Szalay, J. R., Pokorný, P., Malaspina, D. M., Pusack, A., Bale, S. D., Battams, K., et al. (2021). Collisional evolution of the inner zodiacal cloud. *The Planetary Science Journal*, *2*(5), 185. https://doi.org/10.3847/PSJ/abf928

Tao, J., Wang, L., Zong, Q., Li, G., Salem, C. S., Wimmer-Schweingruber, R. F., et al. (2016). Quiet-time suprathermal (0.1-1.5 keV) electrons in the solar wind. *The Astrophysical Journal*, *820*(1), 22. https://doi.org/10.3847/0004-637X/820/1/22

Tkachenko, A., Krasnoselskikh, V., & Voshchepynets, A. (2021). Harmonic radio emission in randomly inhomogeneous plasma. *The Astrophysical Journal*, *908*(2), 126. https://doi.org/10.3847/1538-4357/abd2bd

Tong, Y., Vasko, I. Y., Artemyev, A. V., Bale, S. D., & Mozer, F. S. (2019). Statistical study of whistler waves in the solar wind at 1 au. The Astrophysical Journal, 878 (1), 41. https://doi.org/10.3847/1538-4357/ab1f05

Tong, Y., Vasko, I. Y., Pulupa, M., Mozer, F. S., Bale, S. D., Artemyev, A. V., & Krasnoselskikh, V. (2019). Whistler wave generation by halo electrons in the solar wind. *The Astrophysical Journal Letters*, *870*(1), L6. https://doi.org/10.3847/2041-8213/aaf734

Vasko, I. Y., Krasnoselskikh, V., Tong, Y., Bale, S. D., Bonnell, J. W., & Mozer, F. S. (2019). Whistler fan instability driven by strahl electrons in the solar wind. *The Astrophysical Journal*, *871*(2), L29. https://doi.org/10.3847/2041-8213/ab01bd

Verniero, J. L., Larson, D. E., Livi, R., Rahmati, A., McManus, M. D., Pyakurel, P. S., et al. (2020). Parker solar probe observations of proton beams simultaneous with ion-scale waves. *The Astrophysical Journal Supplement*, *248*(1), 5. https://doi.org/10.3847/1538-4365/ab86af

Verscharen, D., Wicks, R. T., Alexandrova, O., Bruno, R., Burgess, D., Chen, C. H. K., et al. (2021). A case for electron-astrophysics. *Experimental Astronomy*. https://doi.org/10.1007/s10686-021-09761-5

Vocks, C., & Mann, G. (2003). Generation of suprathermal electrons by resonant wave-particle interaction in the solar corona and wind. *The Astrophysical Journal*, *593*(2), 1134–1145. https://doi.org/10.1086/376682

Voshchepynets, A., Krasnoselskikh, V., Artemyev, A., & Volokitin, A. (2015). Probabilistic model of beam-plasma interaction in randomly inhomogeneous plasma. *The Astrophysical Journal*, *807*(1), 38. https://doi.org/10.1088/0004-637X/807/1/38

Zaslavsky, A. (2015). Floating potential perturbations due to micrometeoroid impacts: Theory and application to S/WAVES data. *Journal of Geophysical Research*, *120*(2), 855–867. https://doi.org/10.1002/2014JA020635